Mon. Not. R. Astron. Soc. **381,** 1219–1234 (2007) doi:10.1111/j.1365-2966.2007.12320.x

High mass-loss asymptotic giant branch stars detected by the *Midcourse Space Experiment* in the 'intermediate' and 'outer' Galactic bulge

D. K. Ojha,[1⋆] A. Tej,[1] M. Schultheis,[2] A. Omont[3] and F. Schuller[4]

[1]*Tata Institute of Fundamental Research, Homi Bhabha Road, Colaba, Mumbai 400005, India*
[2]*Observatoire de Besançon, BP 1615, F-25010 Besançon Cedex, France*
[3]*Institut d'Astrophysique de Paris, CNRS, 98bis Bd Arago, F-75014 Paris, France*
[4]*Max Planck Institut fur Radioastronomie, D-53121 Bonn, Germany*

Accepted 2007 August 2. Received 2007 August 2; in original form 2007 May 4

ABSTRACT

We present a study of *Midcourse Space Experiment* (*MSX*) point sources in the Galactic bulge ($|l| < 3^\circ, 1^\circ < |b| < 5^\circ$), observed in the *A*, *C*, *D* and *E* bands (8–21μm), with a total area ∼48 deg^2 and more than 7000 detected sources in the *MSX D* band (15 μm). We discuss the nature of the *MSX* sources [mostly asymptotic giant branch (AGB) stars], their luminosities, the interstellar extinction, the mass-loss rate distribution and the total mass-loss rate in the bulge. The mid-infrared data of *MSX* point sources have been combined with the near-infrared (*J*, *H* and K_s) data of Two Micron All Sky Survey. The cross-identification was restricted to K_s-band detected sources with $K_s \leqslant 11$ mag. However, for those bright *MSX D*-band sources ($[D] < 4.0$ mag), which do not satisfy this criterion, we have set no K_s-band magnitude cut-off. The bolometric magnitudes and the corresponding luminosities of the *MSX* sources were derived by fitting blackbody curves. The relation between $\dot{M}$ and $(K_s - [15])_0$ was used to derive the mass-loss rate of each *MSX* source in the bulge fields. Except for very few post-AGB stars, planetary nebulae and OH/IR stars, a large fraction of the detected sources at 15 μm (*MSX D* band) are AGB stars well above the red giant branch tip. A number of them show an excess in $([A]-[D])_0$ and $(K_s - [D])_0$ colours, characteristic of mass-loss. These colours, especially $(K_s - [D])_0$, enable estimation of the mass-loss rates ($\dot{M}$) of the sources in the bulge fields which range from 10^{-7} to 10^{-4} M$_\odot$ yr^{-1}. Taking into consideration the completeness of the mass-loss rate bins, we find that the contribution to the integrated mass-loss is probably dominated by mass-loss rates larger than 3×10^{-7} M$_\odot$ yr^{-1} and is about 1.96×10^{-4} M$_\odot$ yr^{-1} deg^{-2} in the 'intermediate' and 'outer' bulge fields of sources with mass-loss rates, $\dot{M} > 3 \times 10^{-7}$ M$_\odot$ yr^{-1}. The corresponding integrated mass-loss rate per unit stellar mass is 0.48×10^{-11} yr^{-1}. Apart from this, the various mid- and near-infrared colour–colour and colour–magnitude diagrams are discussed in the paper to study the nature of the stellar population in the *MSX* bulge fields.

Key words: stars: AGB and post-AGB – circumstellar matter – stars: mass-loss – dust, extinction – infrared: stars.

1 INTRODUCTION

Study of the stellar population of the Galactic bulge fields is of prime importance and plays a crucial role in understanding the formation and evolution of the Galaxy. The high-luminosity asymptotic giant branch (AGB) stars are ideal tracers of stellar population in regions of high extinction such as the 'intermediate' and 'outer' Galactic bulge. Intense mass-loss ($\gtrsim 10^{-6}$ M$_\odot$ yr^{-1}) phase has been identified with stars evolving along the AGB phase. Hence, these sources are enshrouded with circumstellar envelopes of dust and gas. The low effective temperatures and thermal emission from warm dust make these stars bright in the infrared. Deep and large-area infrared surveys offer a unique view of the stellar population towards the inner Galaxy as high interstellar extinction hinders the study at optical wavelengths. A combination of mid- and near-infrared data is essential to sample the high mass-loss AGB population. Mid-infrared data are more sensitive to the infrared excess which is a consequence of mass-loss in the AGB stars. With the availability of infrared data from surveys like the Deep Near-Infrared Survey (DENIS;

⋆E-mail: ojha@tifr.res.in

Epchtein et al. 1994), the Two Micron All Sky Survey (2MASS) (Beichman et al. 1998; Skrutskie, Cutri & Stiening 2006), ISOGAL (Omont et al. 2003) and the *Midcourse Space Experiment* (*MSX*) (Price et al. 2001), there have been a large number of studies on the AGB population of the Galactic bulge fields (e.g. Glass et al. 1999; Schultheis & Glass 2001; Glass & Schultheis 2002; Groenewegen & Blommaert 2005). In a recent study, Ojha et al. (2003) have combined the mid- and near-infrared photometry from ISOGAL, DENIS and 2MASS to study the nature of ISOGAL sources in the 'intermediate' Galactic bulge and discuss their mass-loss rates. Further, the data from GLIMPSE II survey (Ed Churchwell, private communication) will provide an excellent opportunity to study the AGB stars in the inner bulge region. However, the sample has to be restricted to high extinction regions owing to saturation effects of the survey. In the present study we have not included GLIMPSE II data as they do not cover the entire 'intermediate' and 'outer' bulge regions selected in this paper. The stellar population study of the inner bulge with GLIMPSE II data will be presented in a future paper. The AGB stars contribute more than 70 per cent towards the enrichment of the dust component of the interstellar medium (ISM) in the solar neighbourhood (Sedlmayer 1994) and hence it is important to study their mass-loss in different parts of the Galaxy. As discussed in Ojha et al. (2003), the total mass returned to the ISM is dominated by mass-loss rates greater than $10^{-6}\,\mathrm{M}_{\odot}\,\mathrm{yr}^{-1}$ and hence the detection of the entire population of the high mass-loss stars becomes important for determination of the total mass returned to the ISM and probably the total mass of the bulge.

In this paper, we report the study of the *MSX* point sources in the 'intermediate' and 'outer' Galactic bulge fields ($|l| < 3^{\circ}, 1^{\circ} < |b| < 5^{\circ}$) with a total area $\sim$48 deg^2 and more than 7000 detected sources in the *MSX D* band (15 μm). Here, the division into the two aforementioned bulge fields is based on the Galactic latitude. The *MSX* bulge fields in the Galactic latitude bins $1^{\circ} < |b| < 2^{\circ}$ and $2^{\circ} < |b| < 5^{\circ}$ are defined as the 'intermediate' and the 'outer' bulge regions, respectively. We restrict our study to the 'intermediate' and 'outer' Galactic bulge because the extinction here is much less and more homogeneous as compared to the inner bulge. The density of the sources in 'intermediate' and 'outer' bulge also reduces the number of spurious associations to the minimum. As shown in Price et al. (2001), uniform sky coverage in the *MSX* bands extends for only the northern latitudes up to $b = 6^{\circ}$ and the higher latitudes (outer Galaxy) are very sparsely sampled. We have restricted the latitude selection such that the fields covered by us are free from the non-uniform sky coverage beyond $|b| > 5^{\circ}$. We have combined the mid-infrared data of the *MSX* point sources with the near-infrared 2MASS data to determine their nature and the interstellar extinction. Most of the sources are AGB stars well above the red giant branch (RGB) tip with high mass-loss. We have determined the luminosities and mass-loss rates of the stellar population in the *MSX* bulge fields.

The outline of the paper is as follows. In Section 2, we present the *MSX* and 2MASS observations and describe the cross-identification between *MSX* and 2MASS sources. In Section 3, we discuss the determination of interstellar extinction in the line of sight of the bulge fields using the isochrone fitting method. The ISOGAL and DENIS associations of the *MSX* sources in the bulge fields are discussed in Section 4. Section 5 presents the derivation of bolometric magnitude (M_{bol}) and luminosity for each star in the bulge fields. In Section 6, we discuss the derivation of mass-loss rates based on $(K_{\mathrm{s}} - [D])_0$ colour and the estimation of the total mass-loss rate in the 'intermediate' and 'outer' bulge. In Section 7, we present the nature of the *MSX* sources from the various colour–colour and colour–magnitude diagrams. We summarize our results in Section 8.

2 OBSERVATIONS AND CROSS-CORRELATION OF *MSX* AND 2MASS SOURCES

We have used the deep *MSX* Point Source Catalogue Version 2.3 (Egan et al. 2003) in this paper. The catalogue (MSXPSC V2.3) lists the sources detected in *MSX* mid-infrared bands *A, C, D* and *E* with $\lambda(\Delta\lambda)$ corresponding to 8.28(3.36), 12.13(1.72), 14.65(2.23) and 21.34(6.24) μm, respectively. MSXPSC V2.3 has several improvements over the initial published catalogue, MSXPSC Version 1.2 (Egan et al. 1999). In this latest version, the photometry is based on co-added image plates, as opposed to single-scan data, which results in improved sensitivity and hence reliability in the fluxes. Comparison with Tycho-2 positions indicates that the positional accuracy, $\sigma = 2$ arcsec at 8 μm, of the new catalogue is better as compared to MSXPSC V1.2. Also, MSXPSC V2.3 is 100 per cent complete in the *A* band (8 μm) and approaches 100 per cent completeness in the other three bands at the survey sensitivity limit of the *MSX* image data ($\sim$0.1 Jy in *A* band, which is more sensitive than the other bands by a factor of $\sim$10) (Egan et al. 2003).

The total number of sources detected in our fields are 29 709, 8125, 7390 and 3380 in the *MSX A, C, D* and *E* bands, respectively. In the study that follows, we have included only good-quality *MSX* data for which the flux quality flags are 3 and 4 (which implies signal-to-noise ratio $\gtrsim 7$). Taking the quality flags into account, the total number of good-quality sources in our fields are 24 035, 2571, 2550 and 866 in the four bands, respectively. The corresponding average source densities are $\sim 5.0 \times 10^2$, $\sim 0.5 \times 10^2$, $\sim 0.5 \times 10^2$ and $\sim 0.2 \times 10^2$ deg^{-2} in the four bands, respectively.

The *MSX* catalogue is more sensitive (by a factor of $\sim$4 in the *A* band) towards the inner Galactic longitudes as compared to the outer longitudes. This is due to the fact that additional maps of regions at $l = 0$ were co-added to the survey data (Sean Carey, private communication). These additional maps are $\sim$4 times more sensitive. This is evident from the inspection of the data sets. Hence, for clarity we have divided the catalogue into two sets for our study: 'inner' zone ($|l| < 0.^{\circ}5$) and 'outer' zone ($0.^{\circ}5 < |l| < 3.^{\circ}0$). The magnitude histograms of the two zones in the *MSX A, C, D* and *E* bands are displayed in Fig. 1. The histograms show the total source counts of the good-quality sources. The 50 per cent completeness limits (as determined from the flux histograms) of the 'inner' zone are 0.08, 0.40, 0.32 and 1.00 Jy for *A, C, D* and *E* bands, respectively. For the 'outer' zone, the 50 per cent completeness limits correspond to 0.16, 1.58, 1.26 and 3.98 Jy for *A, C, D* and *E* bands, respectively.

From the ISOGAL survey, it is seen that a number of the ISOGAL 15-μm sources are AGB stars in the Galactic bulge and the central disc with evidence of mass-loss in majority of the cases (Omont et al. 2003). The mass-loss in AGB stars may be characterized by their 15-μm excess (Omont et al. 1999; Ortiz, Blommaert & Copet 2002; Ojha et al. 2003). The *MSX D* band is close to this wavelength and hence in the study that follows, our prime focus lies on the sources detected in the *D* band. The proportions of *D*-band sources associated with *A*-, *C*- and *E*-band sources are $\sim$100, $\sim$91 and $\sim$33 per cent, respectively.

The near-infrared data used in this paper have been obtained from the 2MASS Point Source Catalogue (PSC) in the three bands, *J* (1.25 μm), *H* (1.65 μm) and K_{s} (2.17 μm). The full-sky 2MASS catalogue covers the entire *MSX* bulge fields. The 2MASS PSC is >99 per cent complete in the absence of confusion at the 10σ sensitivity limit of 15.8, 15.1 and 14.3 mag in the *J*, *H* and K_{s} bands, respectively (Skrutskie et al. 2006). However, the turnover in the source counts in the Galactic plane field occurs nearly 1 mag brighter, because of the effects of confusion noise on the detection

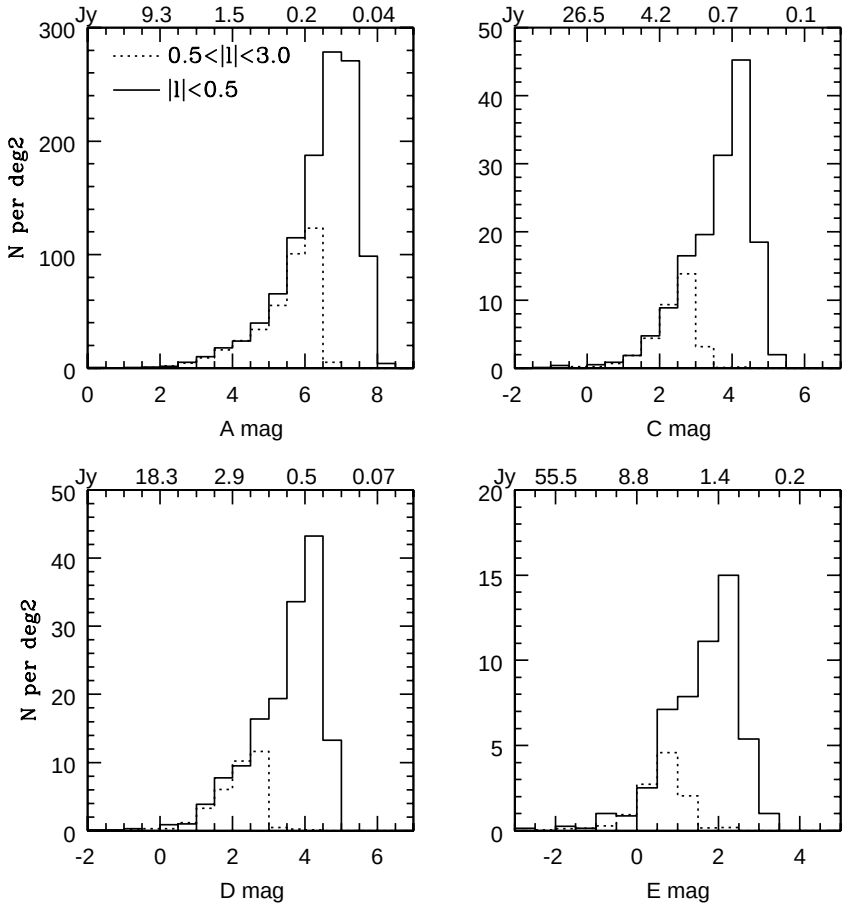

Figure 1. *A*-, *C*-, *D*- and *E*-band source distributions in half-magnitude bins for good-quality (quality flags 3 and 4) *MSX* data. Magnitudes are converted into fluxes using the zero-magnitude flux given by Egan et al. (1999). The solid line denotes the *MSX* sources for the 'inner' zone ($|l| < 0.^{\circ}5$) and the dotted line represents the sources for the 'outer' zone ($0.^{\circ}5 < |l| < 3.^{\circ}0$) in the bulge.

thresholds. The primary areas of confusion are (1) longitudes $\pm 75^{\circ}$ from the Galactic Centre and latitudes 1° from the Galactic plane and (2) within an approximately 5° radius of the Galactic Centre (Skrutskie et al. 2006).

A cross-correlation algorithm similar to the one used by Schuller et al. (2003), to associate the ISOGAL 7- and 15-μm sources with DENIS sources, has been used to search for 2MASS counterparts of the *MSX* point sources in the bulge fields. However, to restrict the number of spurious detections at the fainter end, we set our magnitude cut at conservative brighter level and retain only those 2MASS sources with $K_s \leqslant 11$ mag for cross-correlating with the *MSX* catalogue. This 2MASS magnitude cut ($K_s \leqslant 11$mag) corresponds to an average density of K_s-band sources $n \sim 22\,300$ deg^{-2}. However, the density of $K_s \leqslant 11$ mag sources varies from 18 030 to 26 935 deg^{-2} depending on the locations of the bulge fields. To search for 2MASS counterparts, we assumed a main association radius (r_a) of 4.0 arcsec. The density limit and main association radius are chosen such as to restrict the chance association to less than 10 per cent (where chance association, $y = n\pi r_a^2 \lesssim 0.1$). As a result, ∼89 per cent of the *MSX D*-band sources (2265 sources with quality flags 3 and 4) within the 2MASS observations have an association with a 2MASS source ($K_s \leqslant 11.0$ mag). Also, 2 per cent (48 sources) of the *MSX D*-band sources have a 2MASS counterpart which are saturated ($K_s \lesssim 3.5$ mag). In Fig. 2, we show the 3D plots of the *MSX* source density, the mean A_V and the total number of 2MASS sources ($K_s \leqslant 11.0$ mag) in the various subfields of the bulge as a function of the Galactic longitude and latitude. This information is also presented in tabular form in Table 1, a sample of which is given in this paper.[1]

Keeping in mind the importance of high mass-loss AGB stars in our study, we introduce two additional samples here. We search for 2MASS counterparts of bright *MSX* sources detected in the *D* band but not associated with 2MASS sources with $K_s \lesssim 11.0$ mag. We restrict our sample to sources brighter than 4 mag in the *MSX D* band. This magnitude limit was chosen such as to include all the sources with high mass-loss rates ($\log_{10}(\dot{M})(\mathrm{M}_{\odot}\,\mathrm{yr}^{-1}) \gtrsim -6.0$; see Section 7). There are 165 such sources with good-quality *MSX D*-band photometry. For identifying 2MASS counterparts in this additional sample, we extend the main association radius to a conservative value of ∼5 arcsec without any K_s-band magnitude cut. The increase in the association radius by 1 arcsec enables us to include some known high mass-loss peculiar stars (e.g. carbon stars) in the sample (see Section 7). However, a crucial point is that the removal of the $K_s \lesssim 11.0$ mag cut increases the 2MASS source density to $\sim 10^5$ sources deg^{-2}. Hence, for a main association radius of 5 arcsec, the chance association becomes very large ($y \approx 0.6$) compared to the 10 per cent limit set for the rest of the sources in the bulge fields. The corresponding pure Poisson chance association

[1] Table 1 is available in full in its electronic form via the VizieR Service at the CDS.

Table 1. The detailed characteristics of the sample of *MSX* bulge sublds.

MSX subfileds	*MSX* source density at *D*-band (per deg^2)	Mean A_V (in mag)	δA_V (in mag)	No. of 2MASS sources ($K_s \lesssim 11.0$)	'Foreground' sources[a]	'B' sources[a]
$0.0 < l < 0.5, 1 < b < 2$	808	4.83	1.50	658	36	47
$0.0 < l < 0.5, 2 < b < 3$	530	3.71	1.28	581	29	52
$0.0 < l < 0.5, 3 < b < 4$	304	3.98	1.50	389	26	31
$0.0 < l < 0.5, 4 < b < 5$	72	4.50	1.37	224	14	14

[a]See Section 3 for a description.

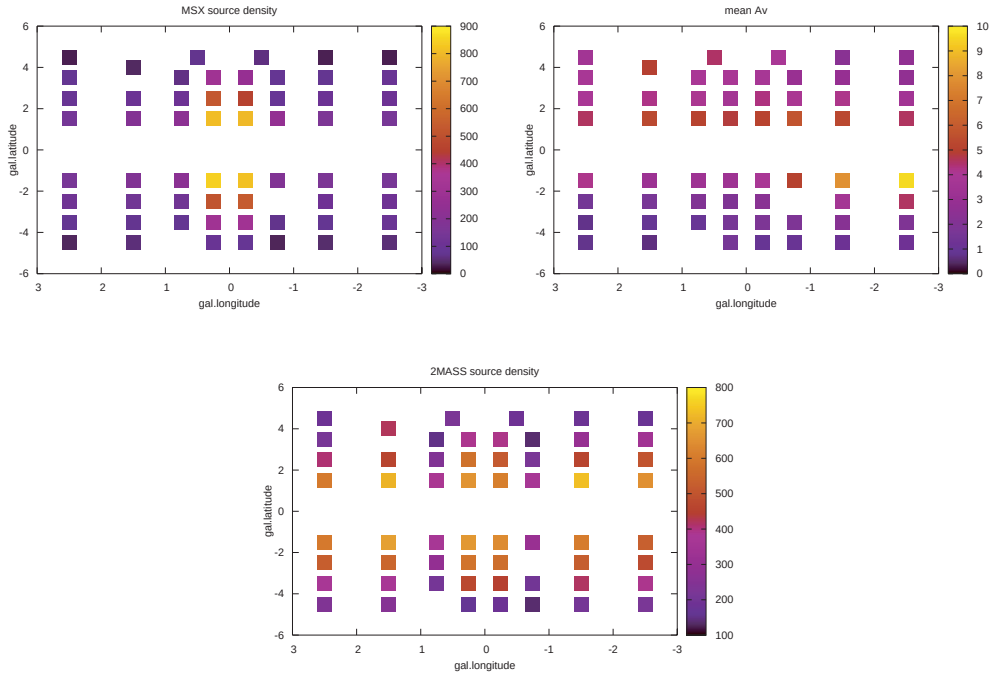

Figure 2. The 3D plots of the *MSX* source density, the mean A_V and the total number of 2MASS sources ($K_s \lesssim 11.0$ mag) in the various subfields of the bulge as a function of the Galactic longitude and latitude. This information in tabular form is presented in Table 1 which is only available in the electronic form via the VizieR Service at the CDS.

Table 2. Sample catalogue of *MSX*–2MASS sources in the bulge fields.

Sequence	Name (MSX6C-)	RA (2000) Dec. (2000) (°)	l b (°)	J (mag)	H (mag)	K_s* K_s** (mag)	[*A*] [7] (mag)	[*C*] (mag)	[*D*] [15] (mag)	[*E*] (mag)	A_V (mag)
6007	G359.9129+02.1610	264.2674	−0.0871	10.11	8.16	6.99	4.15	3.13	2.96	1.99	9.48
		−27.8677	2.1610			7.11	4.72	–	99.99	–	
6057	G359.9338+02.1591	264.2818	−0.0662	7.35	5.81	5.08	3.94	3.04	2.91	2.24	3.98
		−27.8510	2.1591			6.31	4.34	–	99.99	–	
6444	G359.9392+02.0232	264.4150	−0.0608	6.53	5.08	4.30	3.45	2.57	2.51	2.12	3.53
		−27.9193	2.0232			99.99	3.39	–	99.99	–	
6838	G000.3366+02.1338	264.5491	0.3366	9.46	7.94	7.03	4.49	3.50	3.33	2.50	5.50
		−27.5248	2.1338			6.93	99.99	–	3.74	–	
6895	G000.1512+01.9967	264.5683	0.1512	12.05	9.72	8.12	3.95	2.75	2.56	1.70	14.59
		−27.7546	1.9967			8.33	99.99	–	2.45	–	

*2MASS K_s magnitude, **DENIS K_s magnitude; a magnitude of 99.99 means that the source is not detected in the corresponding magnitude band.

is given by $1 - \exp(-y) \approx 0.45$. This implies that about half of the 2MASS associations are likely to be spurious. However, it should be kept in mind that all such spurious associations would possibly have a K_s-band counterpart fainter than the 2MASS limit and hence in our study these sources are retained as a lower limit for K_s band and limit for the high mass-loss end (see Section 6). We are now left with two samples of these bright *MSX* *D*-band sources – (1) sources having a 2MASS counterpart within 5 arcsec radius, which we designate as sample-A and (2) sources having no 2MASS counterpart within this radius, which we name as sample-U. In sample-A, we have

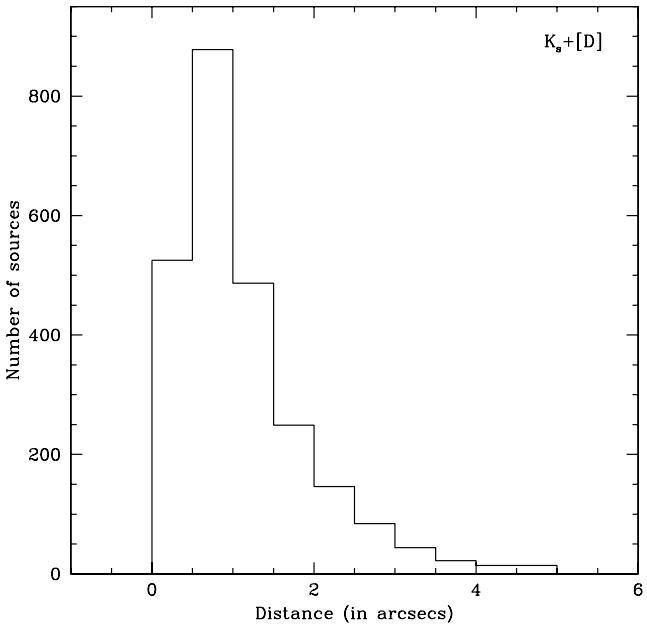

Figure 3. Histogram of positional difference (in arcsec) between good-quality *MSX D*-band (quality flags 3 and 4) and 2MASS cross-identified sources. The *MSX*–2MASS association was limited to $r < 4$ arcsec for bulk of the sources and increased to 5 arcsec for sample-A sources (see the text).

125 sources out of which ∼70 per cent have a single 2MASS association within the 5 arcsec radius. Sample-U contains 42 sources, and we assign a value of $K_s = 13.7$ (which is the K_s-band limit of the sample-A sources) for all these sources.

For this study, along with the good-quality *MSX* band data, we have used only good-quality 2MASS *J*-, *H*- and K_s-band magnitudes with 'rd-flag' values between 1 and 3 which generally implies best quality detection, photometry and astrometry. However, the 2MASS sources with 'rd-flag' value of 6 in the K_s band (which corresponds to a positive detection with an upper magnitude limit) were also included with good-quality sources ('rd-flag' 1–3) for the determination of mass-loss rate only (see Section 6).

In Table 2,[2] we present the full catalogue of *MSX*–2MASS sources from the bulge fields (see Fig. 2 and Table 1), a sample of which is given in this paper. Fig. 3 shows the histogram of positional difference of *MSX D*-band–2MASS cross-identified sources in the bulge fields. The rms of the differences of *MSX*–2MASS association is ∼0.7 arcsec. The histogram peaks at ∼1.0 arcsec and the almost exponential decreasing trend with increasing distance indicates good-quality associations, which implies that the number of spurious associations would be minimal in our cross-correlated sample.

3 INTERSTELLAR EXTINCTION AND FOREGROUND DISC STARS

In most parts of the Galactic bulge, the interstellar extinction is not homogeneous and occurs in clumps, hence, a detailed extinction map is essential in stellar population studies (Schultheis et al. 1999). In spite of the recent improvements in the extinction measurements of the Galactic bulge (Schultheis et al. 1999; Dutra et al. 2001; Indebetouw et al. 2005; Marshall et al. 2006), the determinations are still uncertain. In this paper, the method as described in Ojha et al. (2003) which is based on the procedure outlined in Schultheis et al. (1999) is used to determine the interstellar extinction. The *MSX* catalogue was divided into 60 subfields. This enables in decreasing the effects of variable and patchy extinction present in the entire bulge field. For $|l| < 1\overset{\circ}{.}0$, we have 0.5 deg^2 fields with steps of $0\overset{\circ}{.}5$ in longitude and $1\overset{\circ}{.}0$ in latitude. For rest of the fields, the field size was increased to 1.0 deg^2 with steps of $1\overset{\circ}{.}0$ both in longitude and latitude. This ensures appreciable statistical sample in each field to derive mean A_V. The fact that we use 1 deg^2 subfields to derive extinction gives some dispersion of the order of typically 1.5 mag in A_V (see Table 1). However, at Galactic latitudes greater than 1° (where our fields are located), the clumpiness of interstellar extinction is less prominent (Schultheis et al. 1999). The subfields are listed in Table 1 and the field centres are displayed in the various plots of Fig. 2. Fig. 4 shows the $J - K_s/K_s$ colour–magnitude diagrams for a few selected *MSX* fields presented in Fig. 2 and listed in Table 1.[3] Fig. 5 shows the $J - K_s/K_s$ colour–magnitude diagrams for two sample fields ($-0\overset{\circ}{.}5 < l < 0\overset{\circ}{.}0$, $3^\circ < b < 4^\circ$, $-2\overset{\circ}{.}0 < l < -1\overset{\circ}{.}0$, $-2^\circ < b < -1^\circ$).

As is clearly seen in Figs 4 and 5, the $J - K_s/K_s$ colour–magnitude diagrams of 2MASS sources in the bulge fields show a well-defined red giant and AGB sequence shifted by fairly uniform extinction, with respect to the reference K_{s0} versus $(J - K_s)_0$ of Bertelli et al. (1994) with $Z = 0.02$ and a distance modulus of 14.5 (distance to the Galactic Centre: 8 kpc). However, a point to be noted here is that the intrinsic depth of the bulge is about 0.3 mag (Glass et al. 1995). We have assumed $A_J/A_V = 0.256$ and $A_{K_s}/A_V = 0.089$ (Glass 1999) and calculated the individual extinction values of the 2MASS bulge sources as described in Ojha et al. (2003). The mean A_V value for each field has been determined by a Gaussian fit to the A_V distribution. It should be noted here that owing to low star counts, we have increased the size of some bins (e.g. $0.0 < l < 0.5, 4.0 < b < 5.0$ and $0.5 < l < 1.0, 4.0 < b < 5.0$ are merged into one bin) to estimate the mean extinction values. The details of the subfields, giving the mean A_V, the total number of sources and the statistics of the background and foreground population are listed in Table 1. To derive the dereddened magnitudes for the *MSX* sources, we have used the extinction law – $A_A/A_V = 0.022$; $A_C/A_V = 0.023$; $A_D/A_V = 0.013$; $A_E/A_V = 0.016$ (Messineo et al. 2002).

As seen in Fig. 5, the 2MASS sources with anomalously low values of A_V are probably foreground stars. For each field we empirically define an isochrone 'F' for which we assume that all the sources on the left-hand side of it are foreground stars. Also seen in Fig. 5 and in each of the bulge fields, these foreground stars are around the isochrone with $A_V \sim 0$ mag and are clearly on the left-hand side of the bulk of the stars grouped around the isochrone with mean A_V of the field. These foreground stars will be no longer considered in the following discussions of bulge stars. However, this empirical way of rejecting foreground population does not exclude foreground stars with significant mass-loss.

There are also a number of stars with $J - K_s$ values significantly larger than the bulk of the other stars in each bulge field (right-hand side of the isochrone empirically defined as 'B' in Fig. 5). The sources to the right-hand side of this isochrone are termed as 'B-sources'. We can see three reasons for such an excess in $J - K_s$. (1) Intrinsic $(J - K_s)_0$ excess induced by a large mass-loss,

[2] Table 2 is available in full in the electronic form via the VizieR Service at the CDS.

[3] The $J - K_s/K_s$ colour–magnitude diagrams of 2MASS sources in the bulge fields are available in full in electronic form via the VizieR Service at the CDS.

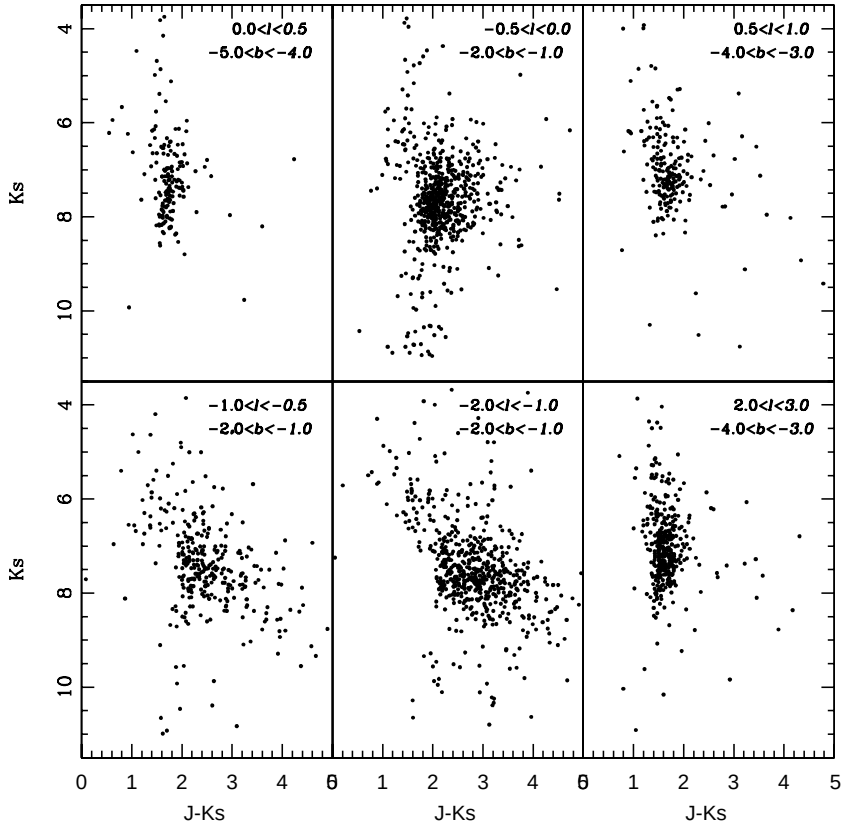

Figure 4. Colour–magnitude diagrams ($J - K_s/K_s$) of 2MASS sources in a few selected *MSX* bulge fields. The complete colour–magnitudes diagrams for all the bulge fields will be available in full in electronic form via the VizieR Service at the CDS.

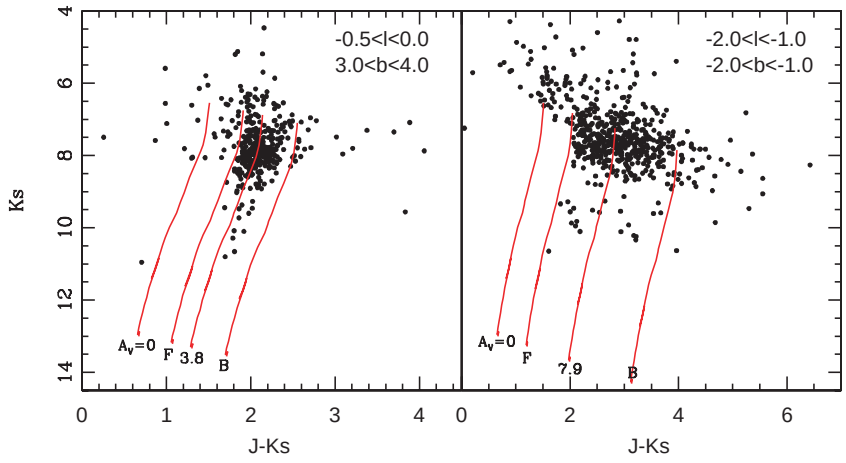

Figure 5. Colour–magnitude diagrams ($J - K_s/K_s$) of *MSX*–2MASS sources in two *MSX* bulge fields. The four isochrones (Bertelli et al. 1994), placed at 8 kpc distance for a 10-Gyr population with $Z = 0.02$ are shown in the figure for $A_V = 0$ mag , for the A_V limit adopted for the 'foreground' sources (defined as 'F'), for mean A_V value of the field and for the A_V limit adopted for the 'B-sources', respectively.

which should be accompanied by a large 15-μm excess. (2) Spurious association or wrong photometry which is rather unlikely for 2MASS sources well above the detection limit. (3) Excess in A_V which should probably be due to a patchy extinction on the bulge line of sight (additional extinction from dust layers behind the Galactic Centre for background stars appears unlikely at such high Galactic latitudes); however, this does not seem a major source of excess with relatively small average extinction. For the bright stars in this region, with $K_s < 8$ mag , we use the mean extinction value (typical $\delta A_V \sim 1.56$mag) of the field. This is because of two reasons: many of the stars with $K_s < 8$ mag should have a large mass-loss which could produce an excess in $(J - K_s)_0$; and at the bright end we are restricted by the limit of the Bertelli et al. (1994) isochrone which is used as the reference in shifting the sources and determining the individual extinctions. For rest of the sources in this region which include the faint sources, with $K_s > 8$ mag , we determine their specific extinction from the $J - K_s/K_s$ colour–magnitude diagram and the zero-extinction isochrone similar to the extinction

determination for the bulk of the bulge sources. For few bright sources in the region on the left-hand side of isochrone 'B', we have extrapolated the Bertelli isochrone to estimate the individual extinction values.

The uncertainties in the estimated values of A_V due to the assumption of a 10-Gyr stellar population of solar metallicity as the reference system has been discussed in Schultheis et al. (1998, 1999). It is shown that the age range (of 5 Gyr) has hardly any effect, whereas, the assumption of solar metallicity results in typical uncertainties of $\sim$1 mag in the determination of A_V. Another important point to be noted here is that for the high mass-loss AGB stars, post-AGB sources and planetary nebula (PN) population, the contribution from the intrinsic extinction due to circumstellar dust has not been considered. This will result in larger uncertainties in the estimated A_V values.

The sample of *MSX* sources discussed in this paper contains $\sim$24 000 2MASS sources which are detected in the K_s band. From this sample we have identified 'foreground' and 'B-sources' based on the method described above and demonstrated in Fig. 5. Their fractions are about 12 per cent (2937) and 9 per cent (2113), respectively. For the sample-A population, we have 111 *MSX* sources (after foreground subtraction) which have good-quality *D* magnitudes (*D*-band quality flags 3 and 4) and K_s-band photometry ('rd-flag' values 1–3). It should be kept in mind that for sample-U sources it is not possible to identify the foreground population and hence, they are not removed from the sample.

4 ISOGAL AND DENIS ASSOCIATION

We have also cross-correlated all the *MSX* sources with the ISOGAL sources in the bulge fields. The ISOGAL Point Sources (Schuller et al. 2003) have been obtained from the VizieR Service at CDS. ISOGAL Point Source Catalogue contains about 10^5 stars, with associated *K*, *J* and *I* DENIS data for most of them (see Schuller et al. 2003). The *MSX* and ISOGAL associations were searched within a radius of 6 arcsec (size of the *ISO* pixel). There are a total of about 2110 ISOGAL sources at 7- and 15-μm in the *MSX* bulge fields (total area $\sim$48 deg^2). Out of this 194 ISOGAL sources at 7 μm have a *MSX A*-band association and 55 ISOGAL sources at 15 μm have *MSX D*-band association. The corresponding magnitude limits for these associated sources are 7.8 and 4.6 mag in the *A* and *D* bands, respectively. We have checked the consistency of *MSX* and ISOGAL 15-μm magnitudes for the 38 strongest sources (with [D] $<$ 4.0 mag; among our sample-A). The average difference is $[15]_{MSX} - [15]_{\rm ISO} = -0.10 \pm 0.43$mag , where the large dispersion is probably related to the source variability. We have searched the DENIS counterparts for only the ISOGAL cross-correlated *MSX* sources. More than 99 per cent of the ISOGAL sources in the bulge fields have a DENIS counterpart. There are 435, 61 and 54 2MASS K_s-band sources which have associations with DENIS K_s-band sources, DENIS K_s and *MSX D*-band sources and DENIS K_s-band, *MSX D*-band and ISOGAL 15-μm sources, respectively. For the ISOGAL cross-correlated sources, we have complemented the 2MASS and *MSX* sources in our catalogue (Table 2) by the DENIS and ISOGAL data. Within the ISOGAL fields (Ojha et al. 2003), more than 95 per cent of *MSX* sources having 2MASS association have an ISOGAL counterpart. We have used the DENIS and ISOGAL data, wherever available, in the estimates of the bolometric magnitudes (see Section 5) and the mass-loss rates (see Section 6) in order to mitigate the effects of variability. Hence, for the bulge sources with DENIS and ISOGAL associations, we have used the average of the 2MASS and DENIS values for the K_s-band magnitude and the *MSX* and ISOGAL 15-μm values for the *D*-band magnitudes.

5 BOLOMETRIC MAGNITUDES AND LUMINOSITIES

After dereddening (see Section 3), the bolometric magnitudes ($M_{\rm bol}$) are derived by integrating the flux densities over the wavelength range between $1.25 < \lambda < 15$ μm by fitting a blackbody curve. For each object we used the dereddened *J*-, K_s-, A-, *D*-band magnitudes and the estimated A_V values as input parameters. The main error of the bolometric corrections results from the interstellar extinction values which gives an error of $\sim$0.2–0.3 mag in $M_{\rm bol}$. The assumption of a blackbody curve for the AGB spectra is less than optimal given the presence of strong molecular bands. We have compared the results obtained from the blackbody fitting with that derived using multiband bolometric correction for AGB stars (Cecile Loup, private communication). However, this method is valid for limited range of colours and luminosities. The difference in $M_{\rm bol}$ derived for from the two methods peaks around $\sim$0.1 mag which is not that significant. As mentioned in the previous section, we have used the average of DENIS and 2MASS K_s-band and *MSX D*-band and ISOGAL 15-μm magnitudes when available. This helps in reducing the uncertainties in $M_{\rm bol}$ and $\dot{M}$ determinations by about a factor of $\sqrt{2}$. At the same time, it is to be noted that large amplitude variable stars such as Miras do show variations in the K_s band up to $\sim$2.5 mag (Glass et al. 2001; Groenewegen 2006). However, the amplitude of intensity variation depends on the period of these sources and is typically in the range 0.5–1.0 mag. Hence, using only single-epoch measurements give us larger errors in the bolometric magnitude determination. The uncertainties due to this variability can only be reduced by obtaining time-consuming light-curve measurements and this is beyond the scope of this present work. It is also important to note that there are 239 ISOGAL 15-μm sources which have not been detected in the *MSX D* band (15 μm) in our sample. These sources have also been used in our sample to determine the $M_{\rm bol}$ and $\dot{M}$. The $M_{\rm bol}$ and luminosity [$L(\mathrm{L}_\odot) = 10^{-(M_{\rm bol}-4.75)/2.5}$] values of each source are given in Table 3,[4] a sample of which is given in this paper. Fig. 6 shows the histograms of bolometric magnitudes and luminosities of the sources in *MSX* bulge fields. The approximate bulge RGB tip is predicted to be at $K_0 \sim 8.0$mag (Frogel, Tiede & Kuchinski 1999) which translates to $M_{\rm bol} \sim -3.5$; $L \approx 2000\,\mathrm{L}_\odot$. This implies that the distributions are clearly incomplete below the luminosity of the bulge RGB tip.

6 MASS-LOSS RATE ($\dot{M}$) IN THE BULGE

We have used the dust radiative transfer models for oxygen-rich AGB stars from Groenewegen (2006) to derive the mass-loss rates of the sources in the *MSX* bulge fields. These models are simulated for values of $L = 3000\,\mathrm{L}_\odot$, distance = 8.5 kpc, expansion velocity = 10 km s^{-1}, dust-to-gas ratio = 0.005, and no interstellar reddening. Our derivations are based on the model for an oxygen-rich AGB star with $T_{\rm eff}$ of 2500 K and 100 per cent silicate composition is used. We have used the empirical relation between $\dot{M}$ and $(K_s - [\mathrm{LW3}])_0$ to determine the mass-loss rate of each star. The luminosity distribution of the sources in our *MSX* bulge fields peaks at $\sim$8000 $\mathrm{L}_\odot$ (see Fig. 6). Using the scaling law given in Groenewegen (2006), we

[4] Catalogue of *MSX* sources from the bulge fields with $\dot{M} > 3 \times 10^{-7}\,\mathrm{M}_\odot\,\mathrm{yr}^{-1}$ is available in full in the electronic form via VizieR Service at the CDS.

Table 3. Sample catalogue of *MSX* sources from the bulge fields with $\dot{M} > 3 \times 10^{-7}\,M_{\odot}\,yr^{-1}$. Data for each source are displayed in two lines, with the *MSX* standard name (e.g. MSX6C-G359.4989−03.301) and the *IRAS* name if any. In order to make the easy comparison with available ISOGAL 7- and 15-μm magnitudes, [7] and [15], and *IRAS* flux densities (in Jy) at 12 and 25 μm, S12 and S25, *MSX* intensities are given in magnitudes for bands *A* (∼8 μm) and *D* (∼15 μm), and in flux densities (in Jy) for bands *C* (∼12 μm) and *E* (∼21 μm).

Name (MSX6C-) *IRAS* name	*l* *b* (°)	*J* (mag)	*H* (mag)	K_s (mag)	[*A*] [7] (mag)	[*D*] [15] (mag)	msxC S12 (Jy)	msxE S25 (Jy)	A_V (mag)	*L* $10^4\,L_{\odot}$	$\dot{M}$ ($M_{\odot}\,yr^{-1}$)
G000.7554−01.0352	0.8	11.17	9.59	8.80	3.27	1.36	4.9	5.8	6.1	0.80	7.0×10^{-6}
17482−2848	−1.0					1.46	5.8	6.6			
G000.0100−03.0215	0.0	12.49	11.92	9.82	2.99	1.59	4.7	4.4	8.7	0.99	6.3×10^{-6}
17543−3027	−3.0					2.54	3.3	3.8			
G359.9506−02.0090	−0.0	14.62	12.21	9.38	2.90	1.34	5.3	5.6	22.6	1.71	2.9×10^{-6}
	−2.0					2.16					
G000.0157+01.6944	0.0	12.92	11.42	10.74	2.75	1.15	5.6	6.3	6.9	1.05	1.6×10^{-5}
17359−2800	1.7						2.9	4.6			
G359.8576+01.0049	−0.1	13.53	11.87	11.19	3.64	1.86	2.7	4.0	8.2	0.51	1.5×10^{-5}
17382−2830	1.0				3.47	1.54	2.0	4.3			

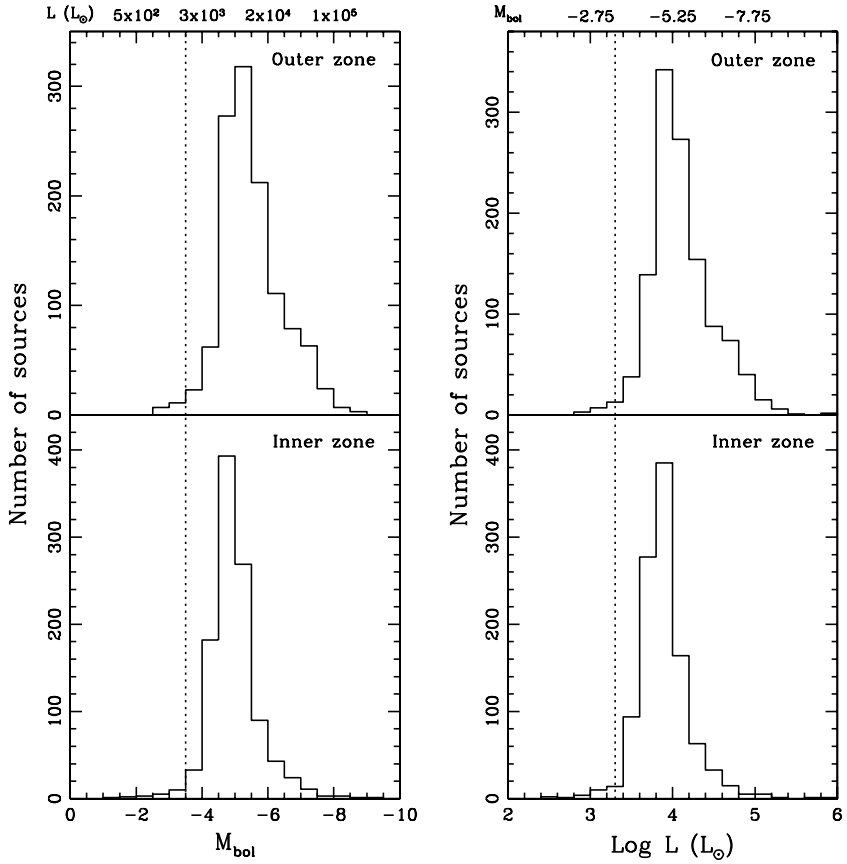

Figure 6. Histograms showing bolometric magnitudes and luminosities of the sources in *MSX* bulge fields which have good-quality (quality flags 3 and 4) *D*-band magnitudes and K_s-band photometry. The dotted vertical lines indicate the approximate bulge RGB tip ($M_{bol} \sim -3.5, L \simeq 2000\,L_{\odot}$).

have scaled the model curve for this peak luminosity. It should be noted that the empirical values tabulated by Groenewegen (2006) are for $\dot{M} < 2 \times 10^{-5}\,M_{\odot}\,yr^{-1}$. For the high mass-loss end (see Fig. 8) we have extrapolated the above empirical relation used by us. It should also be noted here that the mass-loss rate derivations rely on the accurate estimates of the extinction and the corrections applied to the K_s magnitudes. On the other hand, the colour such as $([A] - [D])_0$, which depends little on extinction, allows a direct measure of the mass-loss rates. However, we do not use this colour for mass-loss estimates primarily because it is less sensitive especially for the large and small mass-loss rates. The model based on the synthetic colours of AGB stars by Jeong et al. (2002) has also been used in literature for derivation of mass-loss rate (Ojha et al. 2003). We show a comparison of the Groenewegen's model with that of Jeong et al. (2002) which is significantly different. In Fig. 7, we present the mass-loss rates derived as a function of $(K_s - [LW3])_0$, using the empirical model of Groenewegen (2006) and the empirical relation $\dot{M}$ versus $(K_s - 15)_0$ of Jeong et al. (2002). Here, in place of these

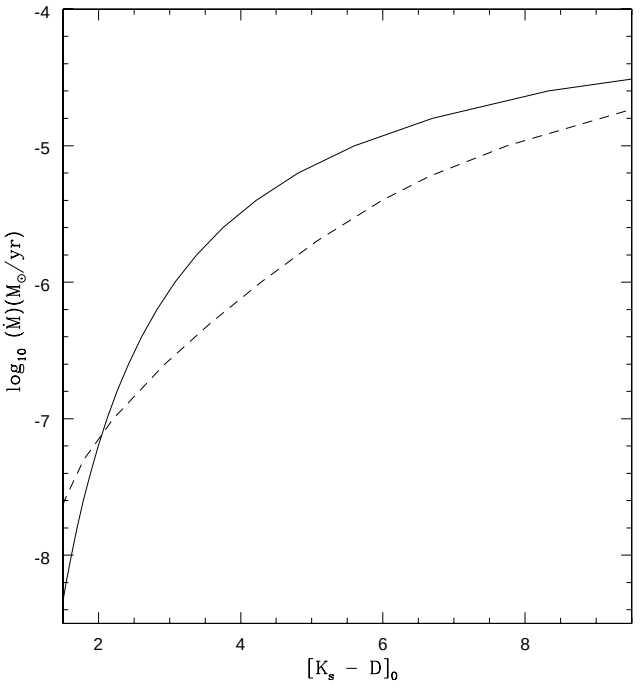

Figure 7. The mass-loss rates as a function of $(K_s - [D])_0$ colour (see text) for the Groenewegen (dotted line) and Jeong (solid line) models.

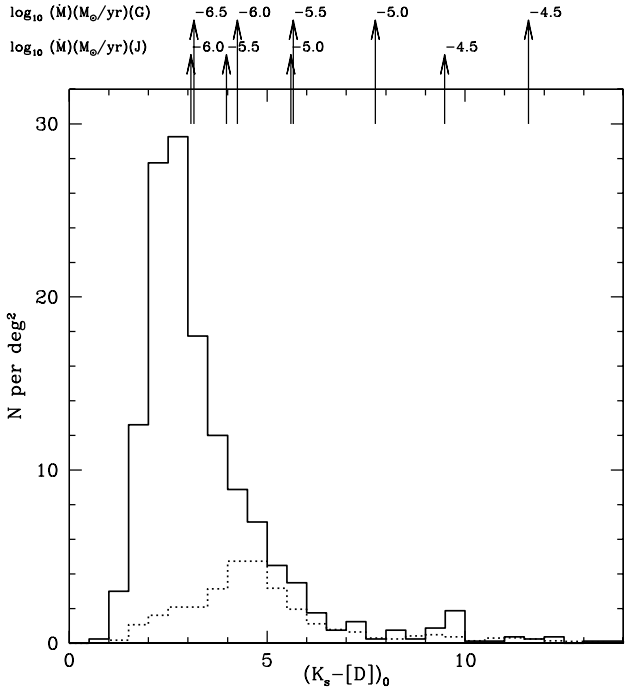

Figure 8. $K_s - [D]$ colour distribution of *MSX* sources. The mass-loss rate scales displayed at the top of the figure are from the models of Groenewegen (upper panel) and Jeong (lower panel). The full line histogram represents the stars of the 'inner' zone ($|l| < 0.^\circ5$) and the dashed line denotes stars of the 'outer' zone ($0.^\circ5 < |l| < 3.^\circ0$) in the bulge (Fig. 2 and Table 1).

colours, we use $(K_s - [D])_0$. This is justified because the central wavelength of *MSX D* band is 14.65 μm which is close to 15 μm and falls within the LW3/*ISO* filter (12–18 μm). It is seen that for Vega the difference in magnitudes ($[D] - [15]$) is 0.04 mag which is negligible. It is to be noticed that in the whole range of mass-loss we are interested in, for $\dot{M} \gtrsim 10^{-7}\,\mathrm{M_\odot\ yr^{-1}}$, the curve based on Groenewegen's model gives lower values of mass-loss by factors of $\gtrsim$3 as compared to the scale of Jeong et al. (2002) for similar colour indices. In this paper, we present the mass-loss rates derived from the models of Groenewegen (2006). The two mass-loss rate scales are also presented later in the discussions of the nature of the *MSX* bulge sources (see Figs 11 and 12).

Fig. 8 shows the $K_s - [D]_0$ colour distribution of *MSX* sources in the 'inner' and 'outer' zones in the bulge fields. There are certain issues regarding the mass-loss estimates which need to be mentioned. It should be noted that using the empirical model of Groenewegen (2006) includes uncertainties in the determination of the mass-loss rates arising from the following reasons. (1) The relation was derived for oxygen-rich AGB stars in the solar neighbourhood. It has also been argued that metallicity affects the dust-to-gas ratio and the outflow velocity from evolved stars (Habing, Tignon & Tielens 1994). This is directly related to the mass-loss and, therefore, the colour-mass-loss relation could possibly differ in different environments such as between the Galactic bulge and the Magellanic Clouds. (2) It is important to emphasize that the AGB stars are variable in nature. The average *K* amplitude of sources associated with known long-period variables (LPVs; Glass et al. 2001) is ∼1.0 mag, which amounts to a factor of ∼2–5 uncertainty in the determination of $\dot{M}$. (3) The model (Groenewegen 2006) used is valid for a limited range of luminosity and expansion velocity and are simulated for AGB stars. Groenewegen (2006) have also mentioned about the caveat of post-AGB model simulation. Here the model for post-AGB sources is calculated under the assumption that the effective temperature and luminosity do not change over the time for the dust shell to drift away. So using the colour–mass-loss relation for sources having these parameters beyond the range (i.e. sources with high luminosity and expansion velocity like PNe and post-AGB or sources with lower luminosity like T-Tauri stars) will have a large uncertainty in their mass-loss estimation. The classical AGB luminosity limit is $\log L(\mathrm{L_\odot}) \sim 4.74$ (Zijlstra et al. 1996; Marigo, Bressan & Chiosi 1998). Hence, in our *MSX* bulge fields, sources having luminosity values beyond this cut-off limit will have larger uncertainties in the mass-loss estimation. These sources and their contribution to the integrated mass-loss rate will be discussed in detail later in this section.

The mass-loss rates for the objects in the *MSX* bulge fields range from 10^{-7} to $10^{-4}\,\mathrm{M_\odot\ yr^{-1}}$. As is obvious from the comparison of the two histograms in Fig. 8, the number of sources is incomplete for $\dot{M} \lesssim 3 \times 10^{-7}\,\mathrm{M_\odot\ yr^{-1}}$ (Groenewegen's model) in the 'inner' zone, and, more severely, for $\dot{M} \lesssim 2 \times 10^{-6}\,\mathrm{M_\odot\ yr^{-1}}$ in the 'outer' zone. The source excess seen particularly in the 'inner' zone for $K_s - [D] \sim 9$– 10, is most likely due to spurious association of the sample-A and sample-U sources (see Section 2), which makes the estimated mass-loss rates appear smaller than their actual values. Numerical values of the mass-loss rates of individual sources are given in Table 3. The number distribution of mass-loss rates in the 'inner' and 'outer' bulge zones as a function of $\dot{M}$ are displayed in Fig. 9. In Fig. 10, we plot the corresponding values of the average total mass-loss rate per square degree and per 0.5 bin of $\log \dot{M}$ for the 'inner' zone. We do not attempt to build the same plot for the 'outer' zone because all the mass-loss bins in this zone, except $\dot{M} \sim 0.3$–$3 \times 10^{-5}\,\mathrm{M_\odot\ yr^{-1}}$, would be very uncertain. This is due to the incompleteness of the lower mass-loss bins and the uncertainty in $K_s - [D]_0$ for $\dot{M} \gtrsim 3 \times 10^{-5}\,\mathrm{M_\odot\ yr^{-1}}$. Numerical values of the integrated mass-loss rate in the 'inner' zone are displayed in Table 4, where we have limited the integration to mass-loss rates, $\dot{M} > 3 \times$

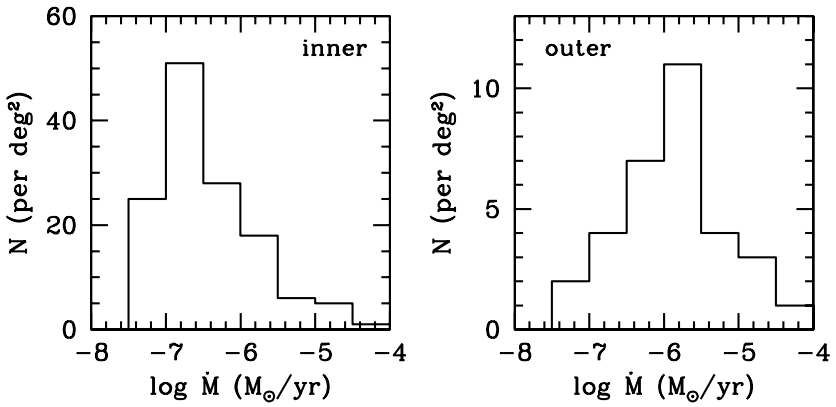

Figure 9. Distribution of mass-loss rates ($\dot{M}$) of *MSX* sources in the 'inner' (left-hand panel) and 'outer' (right-hand panel) bulge zones. The mass-loss rates are inferred from the Groenewegen's model using the $(K_s - [D])_0$ colour.

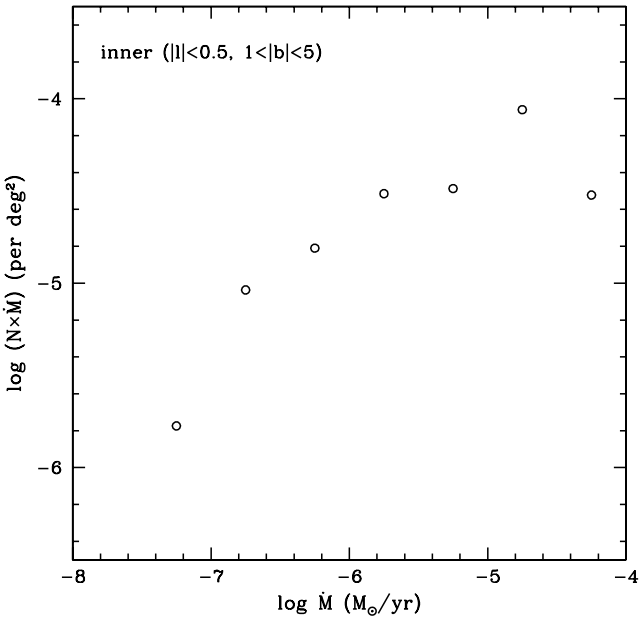

Figure 10. Average total mass-loss rate per square degree and per 0.5 bin of log ($\dot{M}$) as a function of $\dot{M}$ for *MSX* sources in the 'inner' bulge zone.

$10^{-7}\,M_\odot\,yr^{-1}$ for which the data are reasonably complete. The first row shows the value of mass-loss rate per square degree averaged over all the fields in the 'inner' zone. In the next five rows, we give the integrated mass-loss in the five latitude bins which cover the bulge zone. The table also lists the corresponding integrated mass-loss rate per unit stellar mass (in yr^{-1}). The integrated mass-loss rate in the entire 'inner' zone for the bulge fields is $1.96 \times 10^{-4}\,M_\odot\,yr^{-1}\,deg^{-2}$ and the corresponding integrated mass-loss rate per unit stellar mass is $0.48 \times 10^{-11}\,yr^{-1}$ (see Table 4). For the rest of the discussion that follows, it should be kept in mind that the integrated mass-loss rate is only for the 'inner' zone and the contribution from the 'outer' zone is not included.

Here, we would like to discuss about the sources with luminosities beyond the classical AGB limit of $\log L(L_\odot) > 4.74$. There are 18 such sources in the 'inner' zone for which we derive the integrated mass-loss rate. Out of these only three sources have mass-loss rates $\dot{M} > 3 \times 10^{-7}\,M_\odot\,yr^{-1}$. The uncertainty in the mass-loss estimation of these three sources will not affect the integrated mass-loss rate as they contribute less than 4 per cent to the total mass-loss. We have also examined the nature of all these 18 sources in various colour–magnitudes and colour–colour diagrams. Except for one source which has a faint K_s-band magnitude (12.3 mag), rest of sources are very bright in K_s (<5.6 mag) with four of them saturated in 2MASS ($K_s < 3.5$ mag). All of these sources are also bright in the *MSX D* band (<2.8 mag). Referring to Figs 11 and 13, we see that the majority of these sources have blue colours $[(K_s - [D])_0 \sim 2$; $([A] - [D])_0 \sim 1]$. This implies that they are mostly foreground sources which have possibly not been removed using our foreground source rejection procedure (see Section 3). The foreground (or early-type) nature of these sources were further verified in the $(I - J)/(K_s - [D])$ colour–colour diagram based on the discussion presented in Schultheis et al. (2002, cf. fig. 2). Among these 18 sources, there are two sources which show large colour excess in the diagrams discussed above. These are likely to be young stellar objects. Additional spectroscopic and photometric observations are required to understand the nature of these luminous sources. However, the uncertainties involved in the mass-loss rates of these sources do not influence the estimation of the integrated mass-loss rate as their contribution is negligible as is already mentioned.

Table 4. Integrated mass-loss (in $M_\odot\,yr^{-1}\,deg^{-2}$) and integrated mass-loss rate per unit stellar mass (in yr^{-1}) in the 'inner' bulge zone with $\dot{M} > 3 \times 10^{-7}\,M_\odot\,yr^{-1}$. The mass-loss rates are calculated using the model of Groenewegen (2006).

Inner fields	Integrated mass-loss ($M_\odot\,yr^{-1}\,deg^{-2}$)	Integrated mass-loss rate (yr^{-1})
All	1.96×10^{-4}	0.48×10^{-11}
$1\overset{\circ}{.}0 < \|b\| < 1\overset{\circ}{.}5$	4.34×10^{-4}	0.52×10^{-11}
$1\overset{\circ}{.}5 < \|b\| < 2\overset{\circ}{.}0$	3.41×10^{-4}	0.54×10^{-11}
$2\overset{\circ}{.}0 < \|b\| < 3\overset{\circ}{.}0$	1.66×10^{-4}	0.35×10^{-11}
$3\overset{\circ}{.}0 < \|b\| < 4\overset{\circ}{.}0$	1.50×10^{-4}	0.41×10^{-11}
$4\overset{\circ}{.}0 < \|b\| < 5\overset{\circ}{.}0$	0.80×10^{-4}	0.27×10^{-11}

We have also calculated the integrated mass-loss rate for the 'intermediate' ($|l| < 3\overset{\circ}{.}0$, $1^\circ < |b| < 2^\circ$) and the 'outer' ($|l| < 3\overset{\circ}{.}0$, $2^\circ < |b| < 5^\circ$) bulge fields. For $\dot{M} > 3 \times 10^{-7}\,M_\odot\,yr^{-1}$, the integrated mass-loss rates are 3.87×10^{-4} and $1.32 \times 10^{-4}\,M_\odot\,yr^{-1}\,deg^{-2}$ in the two bulge fields, respectively. In comparison, Ojha et al. (2003) derive values of $3.7 \times 10^{-4}\,M_\odot\,yr^{-1}\,deg^{-2}$ and $0.4–1.0 \times 10^{-11}\,yr^{-1}$ for the integrated mass-loss rate and mass-loss rate per unit stellar mass, respectively, using ISOCAM 7- and 15-μm observations. It should be noted here that the

Galactic bulge fields presented in Ojha et al. (2003) cover $-1\overset{\circ}{.}5 < l < +1\overset{\circ}{.}6$, $-3\overset{\circ}{.}8 < b < -1\overset{\circ}{.}0$, $b = +1\overset{\circ}{.}0$ with a total area of $\sim$0.29 deg^2 whereas the area covered in this present work is much larger and hence offers better statistics than the sample of Ojha et al. (2003). The sensitivities of the *MSX* and 2MASS data also allow us to probe the high mass-loss end with a better statistical sample.

Le Bertre et al. (2001, 2003) have studied the Galactic mass-losing AGB stars and concluded that the replenishment to the ISM is dominated ($\gtrsim$50 per cent) by AGB stars with mass-loss rates $\gtrsim 10^{-6}\,M_\odot\,yr^{-1}$. These sources constitute $\sim$10 per cent of their sample and noticeably there are no AGB stars in their sample with mass-loss rates $>10^{-4}\,M_\odot\,yr^{-1}$ though sources with mass-loss $\gtrsim 10^{-4}\,M_\odot\,yr^{-1}$ are known to exist (Habing 1996). The sensitivities of the data sets used by us probe these rare high mass-loss stars. In our *MSX* bulge fields, we have a total of 42 sources displaying mass-loss $\gtrsim 1.0 \times 10^{-5}\,M_\odot\,yr^{-1}$ which significantly contribute to the mass returned to the ISM. In comparison, the stellar population studies in the solar neighbourhood by Jura & Kleinmann (1989) identify 63 sources with mass-loss rates $\gtrsim 10^{-6}\,M_\odot\,yr^{-1}$ out of which only 21 sources in their sample have mass-loss rates $\gtrsim 1.0 \times 10^{-5}\,M_\odot\,yr^{-1}$. From their sample it is seen that oxygen- and carbon-rich AGB stars have almost equal contribution to the replenishment of the ISM which amounts to 3–6 $\times\ 10^{-4}\,M_\odot\,kpc^{-2}\,yr^{-1}$. From the *MSX* bulge fields we estimate the total mass replenishment to the ISM to be $\sim 9 \times 10^{-3}\,M_\odot\,kpc^{-2}\,yr^{-1}$, which is not surprising given the large number of high mass-loss AGB stars ($\dot{M} \gtrsim 1.0 \times 10^{-5}\,M_\odot\,yr^{-1}$) detected in our sample. However, it should also be kept in mind that the sample of Jura & Kleinmann (1989) is incomplete at both the lower and the high mass-loss ends. Since the low mass-loss end is incomplete in our sample, we refrain from making any comparison with other studies.

7 NATURE OF THE *MSX* SOURCES

In this section, we discuss the various colour–magnitude and colour–colour diagrams. This enables us to study the nature of the sources in the *MSX* bulge fields. As has been mentioned earlier, we present only sources with good-quality *MSX* and 2MASS data.

7.1 Colour–magnitude diagrams

In Figs 11–14, we present the dereddened $(K_s - [D])_0/[D]_0$, $(K_s - [D])_0/K_{s0}$, $([A] - [D])_0/[D]_0$ and $(K_s - [A])_0/[A]_0$ colour–magnitude diagrams of *MSX* sources in the two bulge zones, respectively.

Figs 11 and 12 show the two colour–magnitude diagrams involving the $(K_s - [D])_0$ colour which has been used in Section 6 for the derivation of the mass-loss rates of the sources. The mass-loss rate scales derived from Jeong et al. (2002) and Groenewegen (2006) are displayed on the top panel of these two figures. It is interesting to see that the sources from sample-A (which are plotted in red colour) are mostly high mass-loss stars with $(K_s - [D])_0 \gtrsim 6.5$, corresponding to a mass-loss rate $>5 \times 10^{-6}\,M_\odot\,yr^{-1}$ based on the Groenewegen's scale. The sample-U sources (shown in blue) extend the high mass-loss sequence beyond the sample-A sources. It should be kept in mind that the straight line sequence seen for the sample-U sources is partly due to the assigned lower limit of 13.7 mag on the K_s-band magnitude. It is worth recalling here that these two samples constitute sources brighter than 4 mag in *MSX D* band with no 2MASS counterpart with $K_s \lesssim 11.0$ mag within 4 arcsec search radius. Sample-A includes sources having a 2MASS counterpart within an extended 5 arcsec search radius without any K_s-band magnitude cut and sample-U comprises sources having no 2MASS counterpart within this radius. We have assigned $K_s = 13.7$ mag for all the sample-U sources. Another distinct feature which is seen in the 'inner' zone is branching of the sources into two sequences with an appreciable gap around $K_s - [D])_0 \gtrsim 5.5$. It is also interesting to note that majority of the ISOGAL sources seen in the 'inner' bulge zone, i.e. lower luminosity sources, occupy the low mass-loss end of the plots. Our prime focus in this study is to identify the nature of high mass-loss stars in the bulge fields. We therefore selected sources with large mass-loss rates ($>3 \times 10^{-5}\,M_\odot\,yr^{-1}$ as per the Groenewegen's scale) and surveyed the VizieR and SIMBAD data bases for identification with known objects. Since majority of these high mass-loss sources are known *IRAS* (*Infrared Astronomical Satellite*) sources, we used a

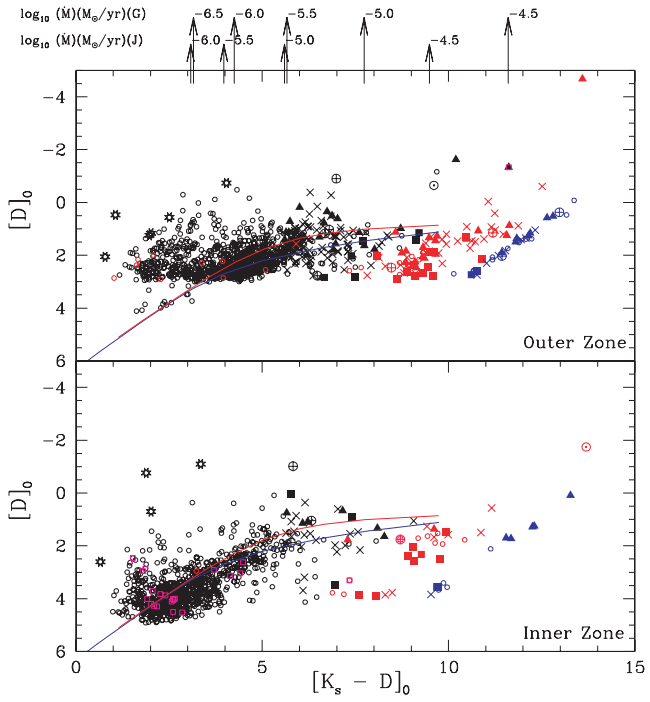

Figure 11. $[D]_0/(K_s - [D])_0$ magnitude–colour diagram for the sources in the *MSX* bulge fields. The upper panel shows the 'outer' zone ($0\overset{\circ}{.}5 < |l| < 3\overset{\circ}{.}0$) and the lower panel shows the 'inner' zone ($|l| < 0\overset{\circ}{.}5$) of the bulge. Only good-quality data (*MSX* flags 3 and 4; 2MASS 'rd-flg' 1–3) are presented. The colour coding which is followed is red for sample-A sources, blue for sample-U sources and black for rest of the bulge fields. The mass-loss rate scales displayed on top are from Groenewegen (2006) and Jeong et al. (2002) (lower) models. The two curves are from the models of Groenewegen (2006), where the red curve represents the model for an oxygen-rich AGB star with $T_{\rm eff} = 2500$ K and a 100 per cent silicate composition. The blue curve is for a carbon-rich AGB star with $T_{\rm eff} = 2650$ K with 100 per cent amorphous carbon (AMC). The model curves are scaled to the peak luminosity of 8000 $L_\odot$ of the sources in the bulge fields. In case of the Groenewegen models, the magnitude in the ISOCAM LW3 (15-μm) filter has been used in place of the *MSX D* band. The ISOGAL counterparts are marked as magenta open squares for the entire bulge fields including the sample-A sources. The known sources from the VizieR and SIMBAD data base are displayed with the following symbols while maintaining the colour coding for the sample-A, sample-U and the rest of the bulge fields sources: PNe and post-AGB stars – solid squares; maser and OH/IR sources – solid triangles; peculiar sources including variable stars – ⊕; *IRAS* sources with no other classifications – crosses. The two carbon stars in our sample are represented by . Sources saturated in the 2MASS K_s band ($\leqslant$3.5) are shown as stars.

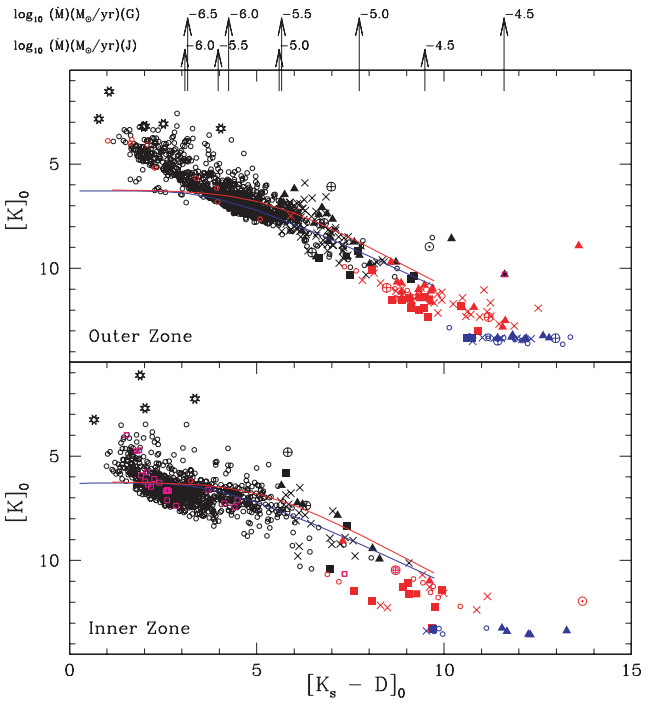

Figure 12. $K_{s0}/(K_s - [D])_0$ magnitude–colour diagram of *MSX* sources with 2MASS counterparts. The symbols are same as shown in Fig. 11.

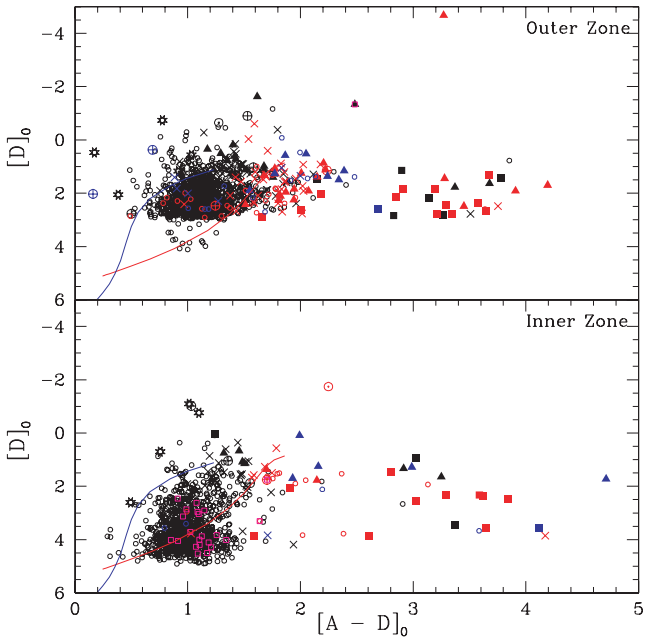

Figure 13. $[D]_0/([A] - [D])_0$ magnitude–colour diagram of good-quality *MSX* sources. The IRAC 8-μm magnitude is used in place of *MSX A* band for the Groenewegen models. The symbols are same as shown in Fig. 11.

search radius of 10 arcsec by taking into consideration the typical *IRAS* PSC error ellipse of ∼10 × 20 arcsec^2. We have grouped these sources identified in VizieR/SIMBAD into four major classes – PNe and post-AGB stars, maser and OH/IR sources, peculiar sources (which also include variable stars) and *IRAS* sources which only have *IRAS* names but no other classifications. We have marked these four classes in the colour–magnitude diagrams using different symbols (see caption of Fig. 11).

In Fig. 13, we have plotted the $([A] - [D])_0/[D]_0$ colour–magnitude diagram. There is a gap seen around $([A] - [D])_0 \sim 2.5$. Among the sources to the right-hand side of this gap (the redder sources) the majority are known post-AGB and PNe. In this figure it is also clearly evident that sources from sample-A are redder than the rest. Fig. 14 shows $(K_s - [A])_0/[A]_0$ colour–magnitude diagram. The $(K_s - [A])_0/[A]_0$ diagram seems to be the best criterion for the detection of large amplitude LPVs (Glass et al. 1999; Schultheis et al. 2000). We see two interesting sequences in this colour–magnitude diagram. The sources seem to branch out into two for $(K_s - [A])_0 \gtrsim 2$, with an appreciable gap between the two. The upper sequence primarily consists of sources with $J - K$ excess and the lower sequence mostly comprises sources which do not have any *D*-band association. Interestingly, the majority of the sources in the lower sequence do not have either *C*- or *E*-band association and are fainter in K_s (>9 mag). The sources from sample-A seem to extend the sequence with increasing slope of the curve with increasing $(K_s - [A])_0$ colour and the majority of these are again known post-AGB and PNe. The sample-U sources seem to form a parallel sequence and occupy the red end. As has been mentioned earlier, it must be noted that this sequence is also a result of the assigned lower limit of 13.7 mag on the K_s-band magnitude of the sources in this sample. In both the above diagrams the ISOGAL sources are towards the blue end.

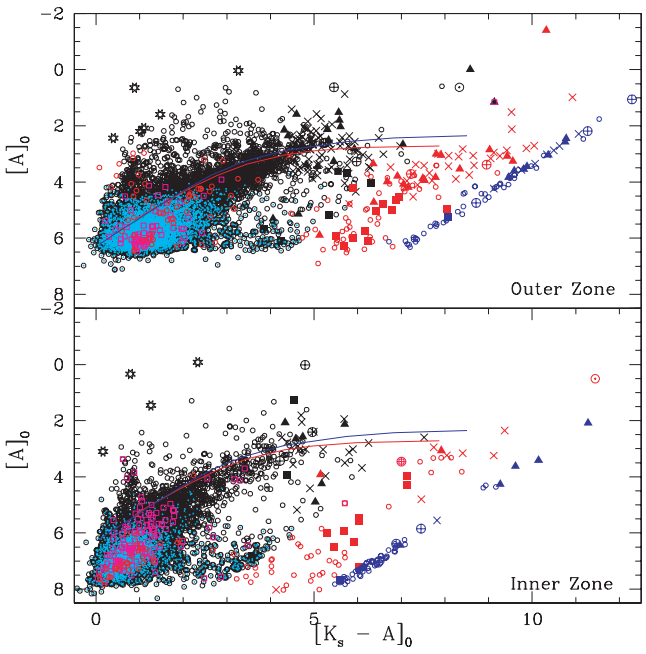

Figure 14. $[A]_0/(K_s - [A])_0$ magnitude–colour diagram of *MSX* sources (quality flags of 3 and 4) with 2MASS counterparts. The upper panel shows the 'outer' zone ($0.^\circ5 < |l| < 3.^\circ0$) and the lower panel shows the 'inner' zone ($|l| < 0.^\circ5$) of the bulge. The symbols are same as in Fig. 11. The cyan circles represent the sources without D associations.

7.2 Colour–colour diagrams

The colour–colour diagrams are also useful for discriminating between different classes of objects and to study their nature. Ortiz et al. (2005), have studied the evolution of carbon- and oxygen-rich AGB stars, post-AGB stars and PNe using mainly data from *MSX*.

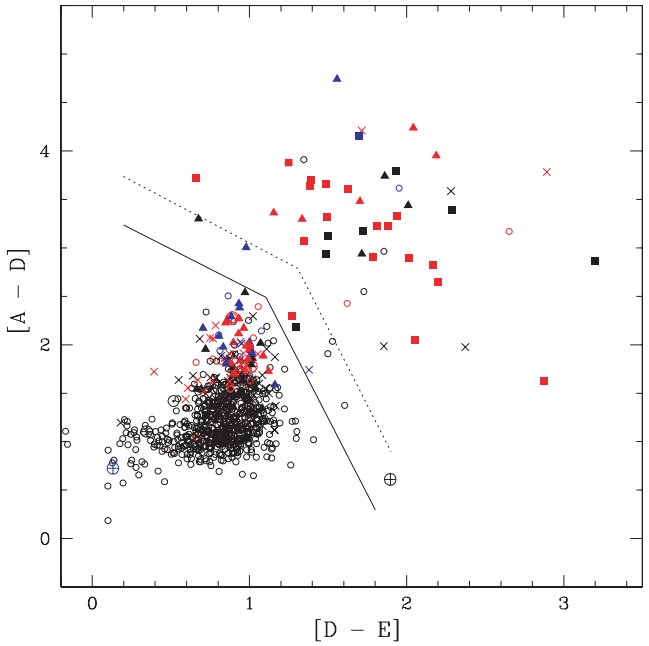

Figure 15. $(D-E)/(A-D)$ colour–colour diagram for the two bulge zones are presented (open black circles). The known objects from the VizieR and SIMBAD data base are displayed. The symbols are same as shown in Fig. 11. The dotted line from Ortiz et al. (2005) shows the position of the gap between. We have added the solid line which allows one to identify a few additional border-line objects

In comparison to their fig. 3, we have plotted the $(D-E)/(A-D)$ colour–colour diagram in Fig. 15. We have plotted the reddened colours to facilitate comparison with the plot of Ortiz et al. (2005). As noted by Ortiz et al. (2005), we also find a distinct gap in the plot which is shown as a solid line based on the visual inspection of our data, in addition to the line (dotted one) from Ortiz et al. (2005). The solid line based on our estimate allows us to discriminate few additional border-line objects. In this figure, we have plotted the known high mass-loss sources, which have already been identified. Apart from these we have also searched the VizieR and SIMBAD data base for known counterparts of all the additional sources lying to the right-hand side of the gap, which were missed out in the earlier selection based on Fig. 11, which included only good-quality K_s-band sources. Majority of the known *IRAS* and maser sources lie to the left-hand lower end of the plot. PNe populate mostly the region beyond the gap. Ortiz et al. (2005) suggest that the gap seen is due to the rapid evolution of stars as they cross the dotted line which can be considered as a transition boundary. This is in good agreement with the different population of sources found on either side of the gap in Fig. 15.

Using *MSX* and 2MASS mid- and near-infrared colour–colour diagrams, Lumsden et al. (2002), Sevenster (2002) and Messineo et al. (2004) have studied different classes of evolved stars with circumstellar envelopes. In Fig. 16, we present the different colour–colour diagrams of the *MSX* bulge fields for good-quality flags in all the *MSX* bands and also in the K_s band. The plots are shown in the units of the reddened flux ratio rather than the colour index for easy comparison with the plots of Lumsden et al. (2002). In Fig. 16(a), we plot the F_{21}/F_8 versus F_8/F_K flux ratios. According to Lumsden et al. (2002), the oxygen- and carbon-rich populations separate out clearly in this colour–colour diagram (see figs 10 and 11 of Lumsden et al. 2002). However, we do not see any such separation here in our *MSX* bulge fields. The OH/IR stars and the PNe mostly have F_{21}/F_8 flux ratios $\gtrsim$1 consistent with the trend seen in fig. 10 of Lumsden et al. (2002). The mid-infrared colours of PNe are similar to H II regions but mostly PNe are bluer because they are not embedded in molecular clouds. Fig. 16(b) shows the F_{12}/F_8 versus F_{21}/F_{14} colour–colour diagram. This diagram is useful to distinguish between the AGB and the post-AGB phases and to locate post-AGB stars which have redder colours due to their colder envelopes (Sevenster 2002; Messineo et al. 2004). The transition from a blue (<2.38) to red (>2.38) F_{12}/F_8 flux ratio may correspond to a transition off the AGB to proto-PNe and from a blue (<1.90) to red (>1.90) F_{21}/F_{14} flux ratio indicates a later evolutionary transition, when mass-loss starts to drop down several order of magnitudes and there is the onset of the fast wind (Messineo et al. 2004). Most of the *MSX* sources show $F_{12}/F_8 < 2.38$ and $F_{21}/F_{14} < 1.90$ as expected for AGB stars. In Fig. 16(c), we plot the F_{21}/F_{14} versus F_{14}/F_8 colour–colour diagram. We do not see any trend separating the oxygen-rich population from the carbon-rich one as pointed out by Lumsden et al. (2002). The majority of the sources are OH/IR stars and *IRAS* sources which occupy the central region of the plot. The PNe are mostly above $F_{21}/F_{14} \gtrsim 1$ and $F_{14}/F_8 \gtrsim 1$. We see a gap around $F_{14}/F_8 \sim 3$. This could possibly suggest the transition from the AGB to the more evolved phase. In Fig. 16(d), we plot the F_{21}/F_8 versus F_{14}/F_{12} flux ratios. The *MSX* sources with $F_{21}/F_8 \gtrsim 5.96$ (see also Fig. 16a) probably represent post-AGB stars (Messineo et al. 2004).

7.3 Population of carbon stars in the bulge fields

We have investigated the nature of the red sources (with $J-K_s>3$) in the various diagrams presented. They occupy the high mass-loss end of Figs 11 and 12 as expected. From the loci of the Groenewegen's models, it is difficult to comment on whether these sources are carbon-rich or oxygen-rich AGB stars. The population of carbon-rich stars if present in the bulge would be crucial in our understanding of the bulge formation, star formation history in the bulge and the nature, formation and evolution of this rare population itself. Except for the peculiar 34 carbon stars detected by Azzopardi et al. (1991), there has been no other carbon star detection in the bulge. The bulge membership and nature of these stars have been a matter of much debate (Whitelock 1993; Ng 1998). In Figs 11 and 12, we see sources falling on the locus of the carbon-rich AGB star model. But based on just the colour and magnitude, it is impossible to confirm or reject the possibility of finding carbon stars in the bulge. Apart from observations focused on the Galactic bulge, there are several other studies based on the near- and mid-infrared colour–colour and colour–magnitude diagrams to identify carbon star populations in different Galactic environments van Loon et al. (1998); Buchanan et al. (2006); Groenewegen et al. (2007); Thorndike et al. (2007). van Loon et al. (1998) have presented the $(H-K)$ versus $(K-[12])$ colour–colour diagram to distinguish between carbon- and oxygen-rich AGB stars. Figs 3(a) and (b) of van Loon et al. (1998) show the Galactic sample of AGB stars from Guglielmo et al. (1993). In their figures, the oxygen- and carbon-rich sequences clearly separate out. In Fig. 17, we have plotted the similar colour–colour diagram $[(H-K_s)/(K_s-C)]$ of the sources in our bulge fields. In this plot we have plotted only sources from sample-A and rest of the bulge fields. Sources from sample-U, which do not have *H*-band magnitudes, are excluded. To compare with the figures of van Loon et al. (1998), we have plotted here the reddened colours. The scatter in our plot makes it difficult to differentiate the two sequences. In their study of luminous sources in the Large Magellanic Cloud (LMC),

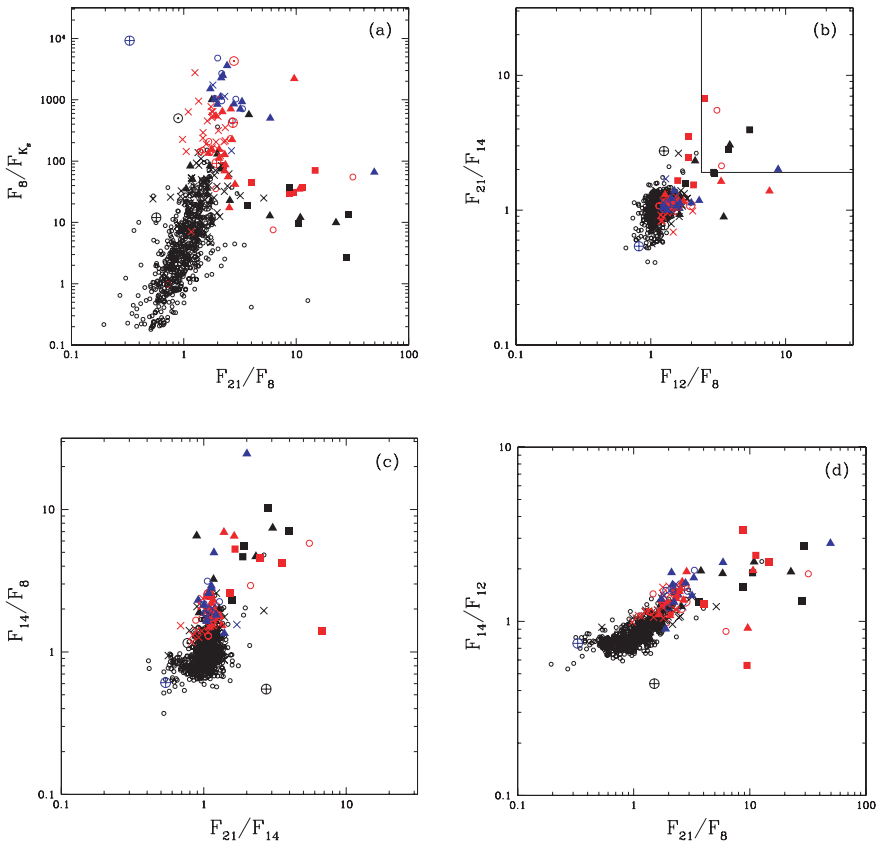

Figure 16. The near- and mid-infrared colour–colour diagrams for the two bulge zones (open black circles). The rectangular box shown in (b) is based on the criteria discussed in Messineo et al. (2004). The symbols are same as shown in Fig. 11.

Thorndike et al. (2007) have used the $(H - K)/(K - [A])$ colour–colour diagram to classify different stellar populations. In Fig. 18, we have plotted a similar reddened $(H - K_s)/(K_s - A)$ colour–colour diagram for the sources in the *MSX* bulge fields. Here also we see the branching off sources into two sequences similar to that seen in Fig. 14. The oxygen- and carbon-rich AGB star models of Groenewegen (2006) trace the sources in the upper sequence better. However, given the scatter in the plot, it is difficult to identify any carbon-rich AGB star sequence as shown in Thorndike et al. (2007). We also derive similar conclusions from the investigation of the $(J - K_s)/(K_s - [A])$ colour–colour diagram (not presented in this paper) based on the plots presented in Buchanan et al. (2006) and Groenewegen et al. (2007). However, it is interesting to note that there are two known carbon stars (IRAS 17534−3030 and IRAS 17547−3249) in our sample, one each in the 'inner' and the 'outer' zone. These sources classified as carbon stars (Volk, Xiong & Kwok 2000; Groenewegen et al. 2002; Guandalini et al. 2006) do not seem to fall on the carbon-rich model curve shown in Figs 11–14. One of the two carbon stars (IRAS 17534−3030), which lies in the 'inner' zone of sample-A, has good-quality 2MASS H, K_s, *MSX A*- and *C*-band data and is shown in Figs 17 and 18. It is seen to lie far away from the carbon line. Here, we would like to recall that for sample-A sources, the chance associations are large (≈0.6; see Section 2) and hence the possibility of a spurious 2MASS association. However, for this particular source which is from sample-A, we have checked the near- and mid-infrared colours in detail. Comparing the colours with the plots presented in Lumsden et al. (2002), we see that the flux ratios agree well with the carbon star population except for the F_{21}/F_8 and F_{21}/F_{12} ratios which are marginally on the redder side.

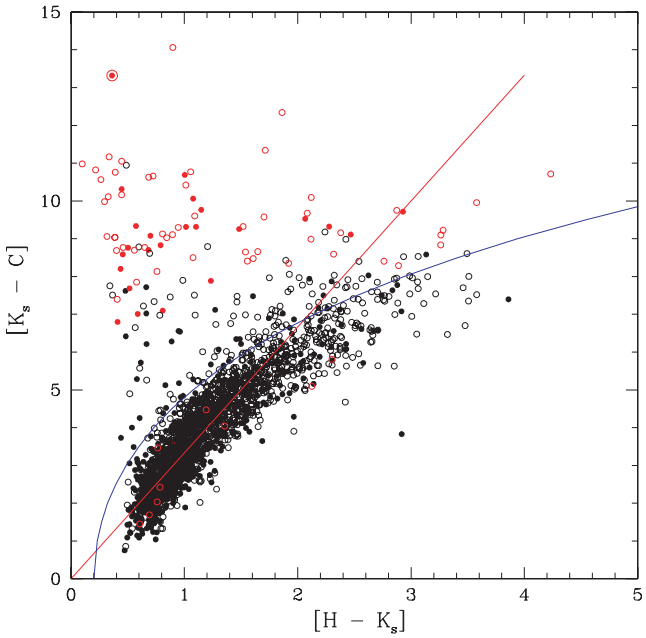

Figure 17. $(H - K_s)/(K_s - [C])$ colour–colour diagram for the 'inner' (solid circles) and 'outer' (open circles) zones are presented. The sources from sample-A are shown in red. The carbon-rich (red line) and oxygen-rich (blue curve) sequences from van Loon et al. (1998) are also plotted. One of the two carbon stars identified in our sample is marked with .

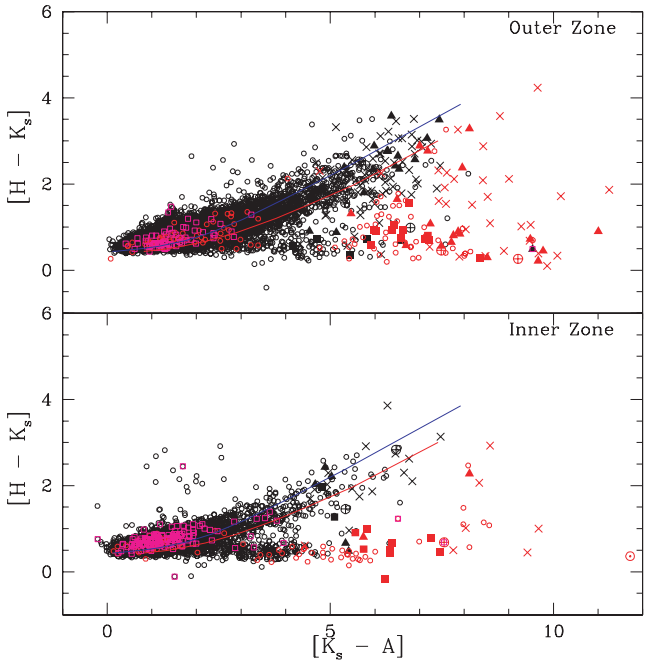

Figure 18. $(H - K_s)/(K_s - [A])$ colour–colour diagram for the 'inner' (solid circles) and 'outer' (open circles) zones are presented. The symbols are same as shown in Fig. 11.

It is worth mentioning here that this carbon star IRAS 17534−3030 is a well-known extreme carbon star which has been recently studied by Pitman, Speck & Hofmeister (2006) using *ISO*-SWS spectra. They predict the possible presence of silicon carbide dust in the star. Apart from this, only near-infrared colour–colour diagrams have also been used to identify carbon stars. Based on the study of Kerschbaum & Hron (1994), we have also checked the $(J - H)$ versus $(H - Ks)$ colour–colour diagram (not presented in this paper). Here also, we are unable to identify any carbon star sequence except for the identified carbon star IRAS 17534−3030 whose $(J - H)/(H - Ks)$ colours are consistent with the locus of carbon stars. Lebzelter, Schultheis & Melchior (2002) and Cioni & Habing (2003), have shown the use of the $(I - J)$ versus $(J - K)$ colour–colour diagram to discriminate between the oxygen- and carbon-rich populations for the LMC. Since most of the sources (including the two known carbon stars) in our sample do not have *I* counterparts, we have not presented this colour–colour diagram in this paper. From the figure of Ortiz et al. (2005), the carbon stars are seen to populate the lower left-hand corner (bluer end – [14.7]–[21.3] colour ranging from ∼0.2 to 0.8 and [8.3]–[14.7] colour ranging from ∼0 to 1.5) of the diagram. One of the two carbon stars in our sample falls in this region (see Fig. 15). Other than this, there is no such distinct population seen among the sources belonging to our bulge fields. We infer that based on only the colour–colour and colour magnitude diagrams we cannot conclusively comment on the presence or absence of carbon stars in the bulge.

8 CONCLUSION

In this paper, we have presented in detail the study of the AGB population detected by *MSX* in the 'intermediate' ($|l| < 3\overset{\circ}{.}0$, $1^\circ < |b| < 2^\circ$) and 'outer' ($|l| < 3\overset{\circ}{.}0$, $2^\circ < |b| < 5^\circ$) Galactic bulge fields covering a large area of 48 deg^2. We have shown that the *MSX* data in conjunction with the 2MASS data base can be potentially used to detect AGB stars well above the RGB tip with the determination of their luminosities (provided they belong to the bulge) and mass-loss rates. The sensitivities of the two surveys enable us to sample the high mass-loss end, characterized by excess in $K_s - [D])_0$ colour due to circumstellar dust emission, with better statistics. We have derived the mass-loss rates of all the *MSX* sources which range from 10^{-7} to $10^{-4}\,M_\odot\,yr^{-1}$ and estimated the integrated mass-loss rate in the *MSX* bulge fields. Taking the completeness into account, we have limited the integration to mass-loss rates, $\dot{M} > 3 \times 10^{-7}\,M_\odot\,yr^{-1}$ for the 'inner' zone ($|l| < 0\overset{\circ}{.}5$) only. There is a factor of ∼3 increase in the estimated integrated mass-loss rate in the 'intermediate' ($3.87 \times 10^{-4}\,M_\odot\,deg^{-2}\,yr^{-1}$) as compared to the 'outer' ($1.32 \times 10^{-4}\,M_\odot\,deg^{-2}\,yr^{-1}$) bulge regions. The average integrated mass-loss rate is estimated to be $1.96 \times 10^{-4}\,M_\odot\,deg^{-2}\,yr^{-1}$ and the corresponding integrated mass-loss rate per unit stellar mass is $0.48 \times 10^{-11}\,yr^{-1}$. Apart from the mass-loss derivations, we have used the various colour–magnitude and colour–colour diagrams to discuss in detail the nature of the *MSX* sources in the bulge fields and identify the location of PNe, post-AGB stars, OH/IR sources, etc. in these diagrams.

Studies based on proposed *Spitzer* IRAC and MIPS photometric surveys of the innermost Galaxy including the most obscured and crowded region would in future enable us to unravel in detail the late stages of stellar evolution particularly of the infrared luminous AGB stars, the mass-loss of which is crucial in understanding the later stellar fate and hence the dust in the Universe. Future infrared mission (e.g. *WISE*; Duval et al. 2004) hold the key to such studies.

ACKNOWLEDGMENTS

We thank the anonymous referee for the comments and suggestions that helped in improving the paper. This publication makes use of data products from the 2MASS, which is a joint project of the University of Massachusetts and the Infrared Processing and Analysis Center/California Institute of Technology, funded by the National Aeronautics and Space Administration and the National Science Foundation.

This research made use of data products from the Midcourse Space Experiment, the processing of which was funded by the Ballistic Missile Defence Organization with additional support from NASA office of Space Science. We would like to thank C. Loup for providing the program to calculate the bolometric magnitudes.

REFERENCES

Azzopardi M., Rebeirot E., Lequeux J., Westerlund B. E., 1991, A&AS, 88, 265

Beichman C. A., Chester T. J., Skrutskie M., Low F. J., Gillet F., 1998, PASP, 110, 480

Bertelli G., Bressan A., Chiosi C., Fagotto F., Nasi E., 1994, A&AS, 106, 275

Buchanan C. L., Kastner J. H., Forrest W. J., Hrivnak B. J., Sahai R., Egan M., Fran A., Barnbaum C., 2006, ApJ, 132, 1890

Cioni M.-R. L., Habing H. J., 2003, A&A, 402, 51

Dutra C. M., Bica E., Clariá J. J., Piatti A. E., Ahumada A. V., 2001, A&A, 371, 895

Duval V. G., Irace W. R., Mainzer A. K., Wright E. L., 2004, in Mather J. C., ed., Proc. SPIE, Vol. 5487, Optical, Infrared, and Millimeter Space Telescopes. SPIE, Bellingham, WA, p. 101

Egan M. P., Price S. D., Moshir M. M., Cohen M., Tedesco E., 1999, MSX Point Source Catalog Explanatory Guide Version 1.2, AFRL-VS-TR-1999-1522, Air Force Research Laboratory, AD-A381933

Egan M. P. et al., 2003, MSX Point Source Catalog Explanatory Guide Version 2.3, AFRL-VS-TR-2003-1589, Air Force Research Laboratory, AD-A381933

Epchtein N. et al., 1994, Ap&SS, 217, 3
Frogel J. A., Tiede G. P., Kuchinski L. E., 1999, AJ, 117, 2296
Glass I. S., 1999, Handbook of Infrared Astronomy. Cambridge Univ. Press, Cambridge
Glass I. S., Schultheis M., 2002, MNRAS, 337, 519
Glass I. S., Whitelock P. A., Catchpole R. M., Feast M. W., 1995, MNRAS, 273, 383
Glass I. S. et al., 1999, MNRAS, 308, 127
Glass I. S., Matsumoto S., Carter B. S., Sekiguchi K., 2001, MNRAS, 321, 77
Groenewegen M. A. T., 1997, in Garzon F., Epchtein N., Omont A., Burton B., Persi P., eds, The Impact of Large Scale Near-IR Sky Surveys. Kluwer, Dordrecht, p. 165
Groenewegen M. A. T., 2006, A&A, 448, 181
Groenewegen M. A. T., Blommaert J. A. D. L., 2005, A&A, 443, 143
Groenewegen M. A. T., Sevenster M., Spoon H. W. W., Pérez I., 2002, A&A, 390, 511
Groenewegen M. A. T. et al., 2007, MNRAS, 376, 313
Guandalini R., Busso M., Ciprini S., Silvestro G., Persi P., 2006, A&A, 445, 1069
Guglielmo F., Epchtein N., Le Bertre T., Fouque P., Hron J., Kerschbaum F., Lepine J. R. D., 1993, A&AS, 99, 31
Habing H. J., 1996, A&AR, 7, 97
Habing H. J., Tignon J., Tielens A. G. G. M., 1994, A&A, 286, 523
Indebetouw R. et al., 2005, ApJ, 619, 931
Jeong K. S., Winters J. M., Le Berte T., Sedlmayr E., 2002, in Nakada Y., Honma M., Sekin M., eds, Astrophys. Space Sci. Library, Mass-Losing Pulsating Stars and Their Circumstellar Matter. Kluwer Academic Publishers, Dordrecht
Jura M., Kleinmann S. G., 1989, ApJ, 341, 359
Kerschbaum F., Hron J., 1994, A&AS, 106, 397
Le Bertre T., Matsuura M., Winters J. M., Murakami H., Yamamura I., Freund M., Tanaka M., 2001, A&A, 376, 997
Le Bertre T., Tanaka M., Yamamura I., Murakami H., 2003, A&A, 403, 943
Lebzelter T., Schultheis M., Melchior A. L., 2002, A&A, 393, 573
Lumsden S. L., Hoare M. G., Oudmaijer R. D., Richards D., 2002, MNRAS, 336, 621
Marigo P., Bressan A., Chiosi C., 1998, A&A, 331, 564
Marshall D. J., Robin A. C., Reylé C., Schultheis M., Picaud S., 2006, A&A, 453, 635
Messineo M., Habing H. J., Sjouwerman L. O., Omont A., Menten K. M., 2002, A&A, 393, 115
Messineo M., Habing H. J., Menten K. M., Omont A., Sjouwerman L. O., 2004, A&A, 418, 103
Ng Y. K., 1998, A&A, 338, 435
Ojha D. K., Omont A., Schuller F., Simon G., Ganesh S., Schultheis M., 2003, A&A, 403, 141
Omont A. et al., 1999, A&A, 348, 755
Omont A. et al., 2003, A&A, 403, 975
Ortiz R., Blommaert J. A. D. L., Copet E., 2002, A&A, 388, 279
Ortiz R., Lorenz-Marins S., Maciel W. J., Rangel E. M., 2005, A&A, 431, 565
Pitman K. M., Speck A. K., Hofmeister A. M., 2006, MNRAS, 371, 1744
Price S. D., Egan M. P., Carey S. J., Mizuno D. R., Kuchar T. A., 2001, AJ, 121, 2819
Schuller F. et al., 2003, A&A, 403, 955
Schultheis M., Glass I. S., 2001, MNRAS, 327, 1193
Schultheis M., Ng Y. K., Hron J., Kerschbaum F., 1998, A&A, 338, 581
Schultheis M. et al., 1999, A&A, 349, 69
Schultheis M. et al., 2000, A&A, 362, 215
Schultheis M., Parthasarathy M., Omont A., Cohen M., Ganesh S., Sevre F., Simon G., 2002, A&A, 386, 899
Schultheis M., Lançon A., Omont A., Schuller F., Ojha D. K., 2003, A&A, 405, 531
Sedlmayer E., 1994, in Jorgensen U. G., ed., Molecules in the Stellar Environment. Springer-Verlag, Berlin, p. 163
Sevenster M. N., 2002, AJ, 123, 2772
Skrutskie M. F., Cutri R. M., Stiening R., 2006, AJ, 131, 1163
Thorndike S. L., Kastner J. H., Buchanan C., Hrivnak B. J., Sahai R., Egan M., 2007, AJ, submitted (astro-ph/0703584)
van Loon J. Th. et al., 1998, A&A, 329, 169
Volk K., Xiong G-Z., Kwok S., 2000, ApJ, 530, 408
Whitelock P., 1993, in De Jonghe H., Habind H. J., eds, IAU Symp. Vol. 153, Galactic Bulges. Kluwer Academic Publishers, Dordrecht, p. 39
Zijlstra A. A., Loup C., Waters L. B. F. M., Whitelock P., van Loon J. Th., Guglielmo F., 1996, MNRAS, 279, 32

This paper has been typeset from a TEX/LATEX file prepared by the author.